

JADES: A Prominent Galaxy Overdensity Candidate within the First 500 Myr

ZIHUAO WU ,¹ DANIEL J. EISENSTEIN ,¹ BENJAMIN D. JOHNSON ,¹ KEVIN HAINLINE ,² WILLIAM M. BAKER ,³ ANDREW J. BUNKER ,⁴ ALEX J. CAMERON ,^{5,6} EMMA CURTIS-LAKE ,⁷ A. LOLA DANHAIVE ,^{8,9} RYAN HAUSEN ,¹⁰ JAKOB M. HELTON ,¹¹ ZHIYUAN JI ,² TOBIAS J. LOOSER ,¹ ROBERTO MAIOLINO ,^{8,9,12} PETRA MENGISTU ,¹³ PIERLUIGI RINALDI ,¹⁴ BRANT E. ROBERTSON ,¹³ FENGWU SUN ,¹ SANDRO TACCHELLA ,^{8,9} JAMES A. A. TRUSSLER ,¹ CHRISTINA C. WILLIAMS ,¹⁵ CHRISTOPHER N. A. WILLMER ,² AND JORIS WITSTOK ,^{5,6}

¹Center for Astrophysics | Harvard & Smithsonian, 60 Garden St., Cambridge MA 02138 USA

²Steward Observatory, University of Arizona, 933 N. Cherry Avenue, Tucson, AZ 85721, USA

³DARK, Niels Bohr Institute, University of Copenhagen, Jagtvej 155A, DK-2200 Copenhagen, Denmark

⁴Department of Physics, University of Oxford, Denys Wilkinson Building, Keble Road, Oxford OX1 3RH, UK

⁵Cosmic Dawn Center (DAWN), Copenhagen, Denmark

⁶Niels Bohr Institute, University of Copenhagen, Jagtvej 128, DK-2200, Copenhagen, Denmark

⁷Centre for Astrophysics Research, Department of Physics, Astronomy and Mathematics, University of Hertfordshire, Hatfield AL10 9AB, UK

⁸Kavli Institute for Cosmology, University of Cambridge, Madingley Road, Cambridge, CB3 0HA, UK

⁹Cavendish Laboratory, University of Cambridge, 19 JJ Thomson Avenue, Cambridge, CB3 0HE, UK

¹⁰Department of Physics and Astronomy, The Johns Hopkins University, 3400 N. Charles St., Baltimore, MD 21218

¹¹Department of Astronomy & Astrophysics, The Pennsylvania State University, University Park, PA 16802, USA

¹²Department of Physics and Astronomy, University College London, Gower Street, London WC1E 6BT, UK

¹³Department of Astronomy and Astrophysics, University of California, Santa Cruz, 1156 High Street, Santa Cruz, CA 95064, USA

¹⁴Space Telescope Science Institute, 3700 San Martin Drive, Baltimore, Maryland 21218, USA

¹⁵NSF National Optical-Infrared Astronomy Research Laboratory, 950 North Cherry Avenue, Tucson, AZ 85719, USA

ABSTRACT

We report a galaxy overdensity candidate at $z \approx 10.5$ in the JWST Advanced Deep Extragalactic Survey (JADES). This overdensity contains 18 galaxies with consistent photometric redshifts and robust F115W dropouts within 8 comoving Mpc in projection. The galaxy number density is four times higher than the field expectation, accounting for one-third of comparably bright galaxies and nearly 50% of the total star formation rate at $10 < z_{\text{phot}} < 12$ in the GOODS-S field. Two compact members of the overdensity show potential Balmer breaks suggestive of evolved stellar populations or little red dots (LRDs). One-third of galaxies have close companions or substructures within 1 kpc at consistent photometric redshifts, implying more frequent interactions in an overdense environment. Most galaxies have stellar masses of $0.6\text{--}3 \times 10^8 M_{\odot}$, half-light radii of ~ 200 pc, and star formation rates of $\sim 5 M_{\odot} \text{ yr}^{-1}$, with no significant deviation from typical high-redshift scaling relations. We find tentative evidence for a spatially varying Ly α transmission inferred photometrically, consistent with an emerging ionized bubble. This overdensity provides a rare opportunity for probing the environmental impact on galaxy evolution and the onset of cosmic reionization within the first 500 Myr.

Keywords: High-redshift galaxies(734)—Reionization(1383)—High-redshift galaxy clusters(2007)

1. INTRODUCTION

Galaxies form and evolve in cosmic large-scale structures shaped by primordial density fluctuations (A. V. Kravtsov & S. Borgani 2012; R. A. Overzier 2016). Despite the remarkable number of galaxies discovered at

$z > 10$ (e.g., E. Curtis-Lake et al. 2023; S. Carniani et al. 2024; M. Castellano et al. 2024; R. P. Naidu et al. 2025; J. Witstok et al. 2025a), none have yet been observed within a significant overdensity at such early epochs.

Overdensities are regarded as progenitors of galaxy clusters in the local Universe. They are often referred to as protoclusters when considered dense enough to eventually collapse into a galaxy cluster, although this design-

nation is mainly practical in simulation contexts (R. A. Overzier 2016). At high redshifts, galaxy overdensities are not gravitationally bound, as their central halos have not grown massive enough (R. H. Wechsler & J. L. Tinker 2018). Their structures therefore trace peaks of the primordial density field (J. M. Bardeen et al. 1986).

Overdensities are the primary sites of star formation in the early Universe. Cosmic structure formation is biased such that massive dark matter halos preferentially form in clustered environments (Y.-K. Chiang et al. 2017; R. H. Wechsler & J. L. Tinker 2018). Consequently, overdensities usually host the most massive galaxies and dominate early stellar mass assembly (P. A. Thomas et al. 2023). Their contribution to the cosmic star formation rate rises from negligible at low redshift to $\sim 50\%$ at $z \gtrsim 5$ (Y.-K. Chiang et al. 2017; S. Lim et al. 2024; F. Sun et al. 2024).

Beyond hosting the most massive halos, overdense environments may further accelerate galaxy formation and evolution (W. M. Baker et al. 2025a; T. Morishita et al. 2025a; C. Witten et al. 2025b). Star formation in overdensities is enhanced at early epochs due to higher gas inflow (J. M. Helton et al. 2024a; Z. Li et al. 2025; T. Morishita et al. 2025a). This enhanced star formation facilitates metal enrichment (Z. Li et al. 2025), although it may be diluted by accretion of metal-poor gas (Z. Li et al. 2022; X. Wang et al. 2022; K. Wang et al. 2023; T. Morishita et al. 2025b). The overdense environment also fosters galaxy mergers and interactions, accelerating the buildup of stellar mass (P. Behroozi et al. 2019).

Overdensities play an important role in cosmic reionization (A. Saxena et al. 2023; J. Witstok et al. 2024; Z. Chen et al. 2025; J. Witstok et al. 2025b). Reionization is thought to proceed through the growth and percolation of ionized bubbles produced by early galaxies (O. Zahn et al. 2007). The detection of Ly α emission at $z = 13$ suggests that such ionized bubbles are already in place at this epoch (J. Witstok et al. 2025a). However, a tension arises regarding the role of overdensities in cosmic reionization: on the one hand, they host more ionizing sources and thus may produce the largest ionizing bubbles; on the other hand, the higher gas density increases hydrogen recombination rates, which may inhibit ionization (S. R. Furlanetto et al. 2004; I. T. Iliev et al. 2006; A. Mesinger & S. Furlanetto 2007; G. Kulkarni & T. R. Choudhury 2011; M. Castellano et al. 2016; R. Endsley & D. P. Stark 2022; R. L. Larson et al. 2022; E. Leonova et al. 2022; T.-Y. Lu et al. 2024; M. Neyer et al. 2024; M. Almualla et al. 2025).

Several overdensities have been spectroscopically identified up to $z \approx 8$ (e.g., M. Ishigaki et al. 2016; W. Hu et al. 2021; N. Laporte et al. 2022; T. Hashimoto et al.

2023; T. Morishita et al. 2023; J. M. Helton et al. 2024b; Y. Fudamoto et al. 2025a,b; Q. Li et al. 2025a,b; T. Morishita et al. 2025b; C. Witten et al. 2025a), indicating that proto-cluster environments were already in place at these epochs. At $z > 10$, however, overdensities remain rare despite the growing number of individual galaxy detections. The only candidate is a moderate overdensity near GN-z11 (S. Tacchella et al. 2023; J. Scholtz et al. 2024), whose statistical significance has yet to be firmly established.

We report the discovery of a prominent overdensity candidate at $z \approx 10.5$. It contains 18 galaxies with consistent photometric redshifts within a radius of 3 arcmin. For comparison, the candidate proto-cluster near GN-z11 only contains six objects with comparable brightness. The number of member galaxies in this overdensity even exceeds most known overdensities at $z \approx 7$ (e.g., J. M. Helton et al. 2024b). We examine the impact of this overdense environment on galaxy properties and discuss the implications for cosmic reionization. This study adopts a Λ CDM cosmology with $H_0 = 68 \text{ km s}^{-1} \text{ Mpc}^{-1}$, $\Omega_m = 0.31$, and $\Omega_\Lambda = 0.69$ according to the full-mission Planck measurements (Planck Collaboration et al. 2020). In this cosmology, 1 arcsec corresponds to 4 proper kpc (pkpc) and 48 comoving kpc (ckpc) at $z = 10.5$.

2. THE OVERDENSITY

The overdensity is found in the GOODS-S field. Deep imaging observations were obtained primarily through the JADES Guaranteed Time Observations (GTO) programs (D. J. Eisenstein et al. 2023) and the JADES Original Field (JOF) program 3215 (D. J. Eisenstein et al. 2025), with additional data from JWST programs 2514, 3990, 5997, and 6434 (C. C. Williams et al. 2025; T. Morishita et al. 2025c; F. Sun et al. 2025; Looser et al. in prep.). The overdensity region corresponds to the JADES medium-depth field and is covered by 9–14 NIRCam bands, with a typical exposure time of 6 hours per band. Our analysis uses the latest JADES DR5 NIRCam imaging products (B. D. Johnson et al. submitted) and the NIRCam source catalogs (B. E. Robertson et al. submitted). The 7σ point-source depth in F115W in this region is $\sim 8 \text{ nJy}$ (B. D. Johnson et al. submitted; B. E. Robertson et al. submitted), similar to that achieved across most of the JADES medium-depth field. The deep F115W imaging provides a robust selection of galaxies at $z \gtrsim 10$ through Ly α dropouts.

We identify the overdensity from a photometric redshift catalog of $z > 8$ candidates in a companion paper (K. N. Hainline et al. submitted). They estimate photometric redshifts using the EAZY software (G. B.

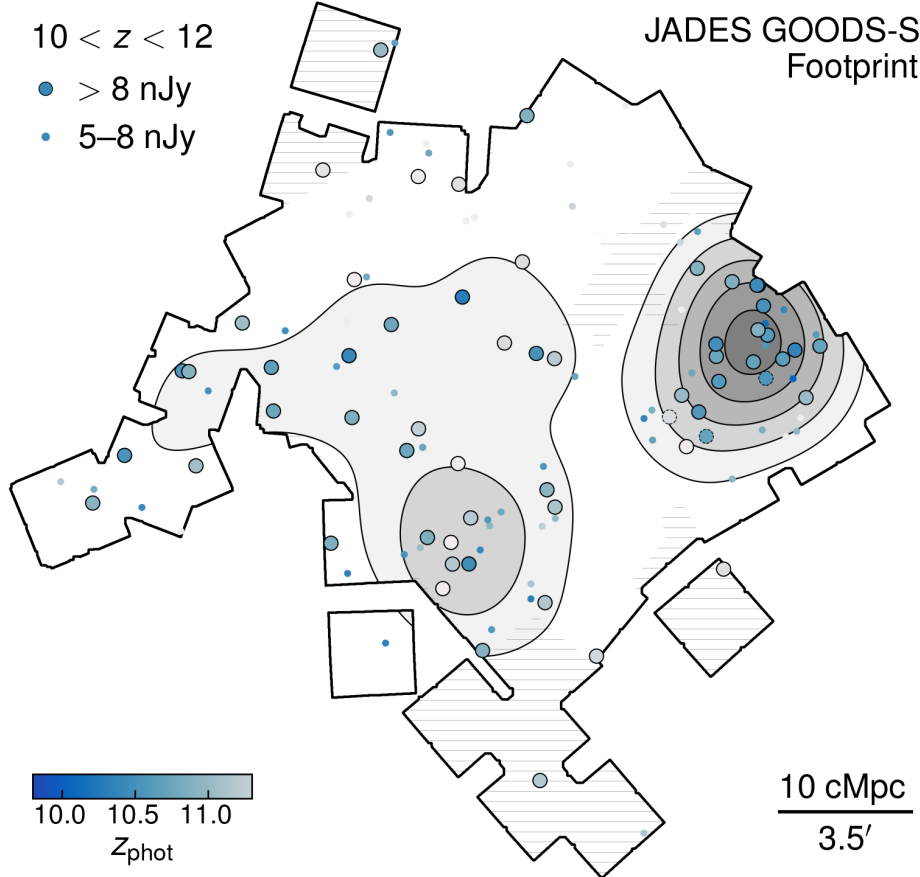


Figure 1. Spatial distribution of galaxy candidates at $10 < z_{\text{phot}} < 12$ from the JADES photometric sample, color-coded by photometric redshift derived with the `EAZY` package. Large circles mark bright sources with F356W fluxes above 8 nJy (29.1 AB mag); small circles mark sources between 5 and 8 nJy. The bold black polygon outlines the JADES/NIRCam GOODS-S footprint in F115W. Hatched regions indicate shallow F115W coverage; all other areas within the footprint reach a point-source depth of 8 nJy at $> 7\sigma$ significance (B. D. Johnson et al. submitted). Contours show the estimated density field at the mean density and 1σ , 2σ , 3σ , and 4σ above the mean density of bright sources, derived with a kernel density estimator following J. M. Helton et al. (2024b). The overdensity is on the west side of the field, with a peak galaxy number density exceeding four times the mean. Three less secure objects within the overdense region, shown as large circles with dashed outlines, are excluded from the density estimate and subsequent analysis and are discussed in Appendix B. North is up, and east is to the left.

Brammer et al. 2008) based on source identification and photometry from the JADES DR5 NIRCam source catalog (B. E. Robertson et al. submitted). To ensure robust photometric redshifts, K. N. Hainline et al. (submitted) further require the sources to have a signal-to-noise ratio (SNR) > 5 in at least two photometric bands, and a $\Delta\chi^2 > 4$ between the $z_{\text{phot}} > 10$ solution and any $z < 7$ solution. We refer to K. N. Hainline et al. (submitted) for details of the photometric redshift selection. Figure 1 shows the spatial distribution of sources at $10 < z_{\text{phot}} < 12$ that are brighter than 8 nJy in F356W. We restrict attention to these bright sources because they have high signal-to-noise detections and more secure redshift constraints. Compared to shorter-wavelength bands, F356W traces star forma-

tion on longer timescales (C. Conroy 2013) and is less sensitive to dust attenuation and metal emission lines. Three sources near the overdensity, marked as blue circles with dashed edges in Figure 1, have $\sim 2.5\sigma$ detections in F115W and thus could be at $z < 10$. Given the ambiguity of this SNR regime, we exclude these objects from the overdensity sample and all subsequent analyses. Their properties are discussed in Appendix B.

The overdensity appears as a concentration of galaxies on the west side of the JADES GOODS-S field (dark gray area in Figure 1). Within the mean-density contour, it contains 18 galaxies with clear Ly α dropout signatures and consistent photometric redshifts near $z_{\text{phot}} = 10.5$. Given its proximity to the edge of the footprint, the overdensity may have more members beyond

the observed area. The overdensity is not an artifact of selection bias since this area has depth and band coverage similar to the majority of the JADES field (B. D. Johnson et al. submitted). Except for a few hatched areas in Figure 1, the JADES GOODS-S field has a depth of 8 nJy at $> 7\sigma$ significance in F115W, ensuring robust Ly α dropout selection for sources brighter than 8 nJy across the entire field. Neither the photometric-redshift criteria nor the flux threshold preferentially increase the number of detections in the overdensity region.

The overdensity far exceeds expectations from a random Poisson distribution. The region contains 18 galaxies within an area of $\sim 15 \text{ arcmin}^2$, whereas the entire GOODS-S field spans 209 arcmin^2 and has only 56 objects under the same selection, including those in the overdensity. Therefore, the significance of the overdensity is $\delta_{\text{gal}} = \rho_{\text{gal}}/\langle \rho_{\text{gal}} \rangle - 1 = 3.5$, implying a galaxy surface density ~ 4 times higher than the field average. Comparing with the luminosity function derived from multiple programs in D. J. McLeod et al. (2024), we find a similar overdensity significance of $\delta_{\text{gal}} = 3.6$, for the photometric redshift interval $\Delta z_{\text{phot}} \sim 1$ within the overdensity. Assuming Poisson statistics for galaxy counts, this corresponds to a 7σ deviation from the mean, where the standard deviation is $\sigma = \sqrt{\langle \rho_{\text{gal}} \rangle}$. This highly significant excess indicates a prominent overdensity. It also implies that statistical studies based on photometric redshift selection are robust, as the expected number of field contaminants is four galaxies, corresponding to $\sim 20\%$ of the overdensity population.

The overdensity is unlikely to be mimicked by a concentration of Balmer-break galaxies at $z = 2\text{--}3$. First, it is extremely rare for stellar Balmer breaks to produce such significant dropout signatures. The median flux ratio of F115W($< 84\%$)/F150W is 0.051, considering the Bayesian 84% upper limit of the F115W flux assuming a non-negative uniform prior (Eisenstein et al. in prep.). Such flux ratios far exceed normal Balmer breaks (A. Mintz et al. 2025). Second, we find no evidence for clustering of $z = 2\text{--}3$ galaxies in this region. Third, given their faintness, many galaxies would likely be satellites at low redshift, especially in cluster environments. We therefore search for potential central galaxies within $3''$ of each source, but the number of bright neighbors (F356W $> 20 \text{ nJy}$) is consistent with a random distribution. These considerations further reinforce the interpretation that the overdensity lies at high redshifts.

3. GALAXY PROPERTIES

3.1. *Measurement*

We perform photometry and structural decomposition using the **ForcePho** package (B. D. Johnson in prep.;

see also B. E. Robertson et al. 2023; S. Tacchella et al. 2023; W. M. Baker et al. 2025b). **ForcePho** models the targets and their subcomponents each with a Sérsic profile and samples model parameters using the Hamiltonian Monte Carlo Markov Chain (MCMC) method. It uses individual exposure images with dithering to achieve subpixel resolution, providing robust size measurement of even barely resolved objects. We simultaneously fit multiband NIRCam images with a common Sérsic model convolved with corresponding point spread functions (PSFs) from STPSF (Version 2.0.0; M. D. Perrier et al. 2014). For computational efficiency, **ForcePho** approximates the PSF as a mixture of six Gaussians, a simplification whose impact has been found to be negligible for faint sources (W. M. Baker et al. 2025b). We adopt flat priors for the Sérsic indices from 0.2 to 8 and for the half-light radii from 1 mas to 1 arcsec. For galaxies with substructures, we visually identify individual components and fit them with separate Sérsic models. Results of the photometry are presented in Table A1.

We perform spectral energy distribution (SED) fitting on the multiband photometry with the **Prospector** software (B. D. Johnson et al. 2021). Redshifts are treated as free parameters, and we consider IGM absorption according to P. Madau (1995). We do not include damped Ly α absorption (DLA) because it is unconstrained by the photometric data and not well understood in over-dense environments. Considering typical DLA effects may lower the inferred redshift by ~ 0.2 (K. N. Hainline et al. submitted). We model the stellar populations using Flexible Stellar Population Synthesis (FSPS; C. Conroy et al. 2009) with Mesa Isochrones and Stellar Tracks (MIST) isochrones (J. Choi et al. 2016) assuming a G. Chabrier (2003) initial mass function in the $0.08\text{--}120 M_{\odot}$ mass range. We adopt a ten-bin non-parametric star formation history (SFH) with the first bin covering a look-back time of 0–5 Myr and the remaining bins logarithmically spaced up to $z = 20$. We adopt a simulation-motivated rising SFH prior following Z. Wu et al. (2025) to account for the expected rising SFHs at high redshifts (C. Turner et al. 2025). We model birth-cloud dust attenuation associated with young stars following S. Tacchella et al. (2022) and galaxy-scale dust with flexible attenuation curves (M. Kriek & C. Conroy 2013). Nebular emission is computed self-consistently with the photoionization code **CLOUDY** (N. Byler et al. 2017). By default of **Prospector**, the “frac_obrun” parameter (N. Byler et al. 2017) is set to zero to prevent overfitting. We assume flat priors for gas-phase metallicity and ionization parameter in log space. To account for uncertainties in Ly α radiative transfer and IGM transmission, we allow the Ly α line intensity to vary via a

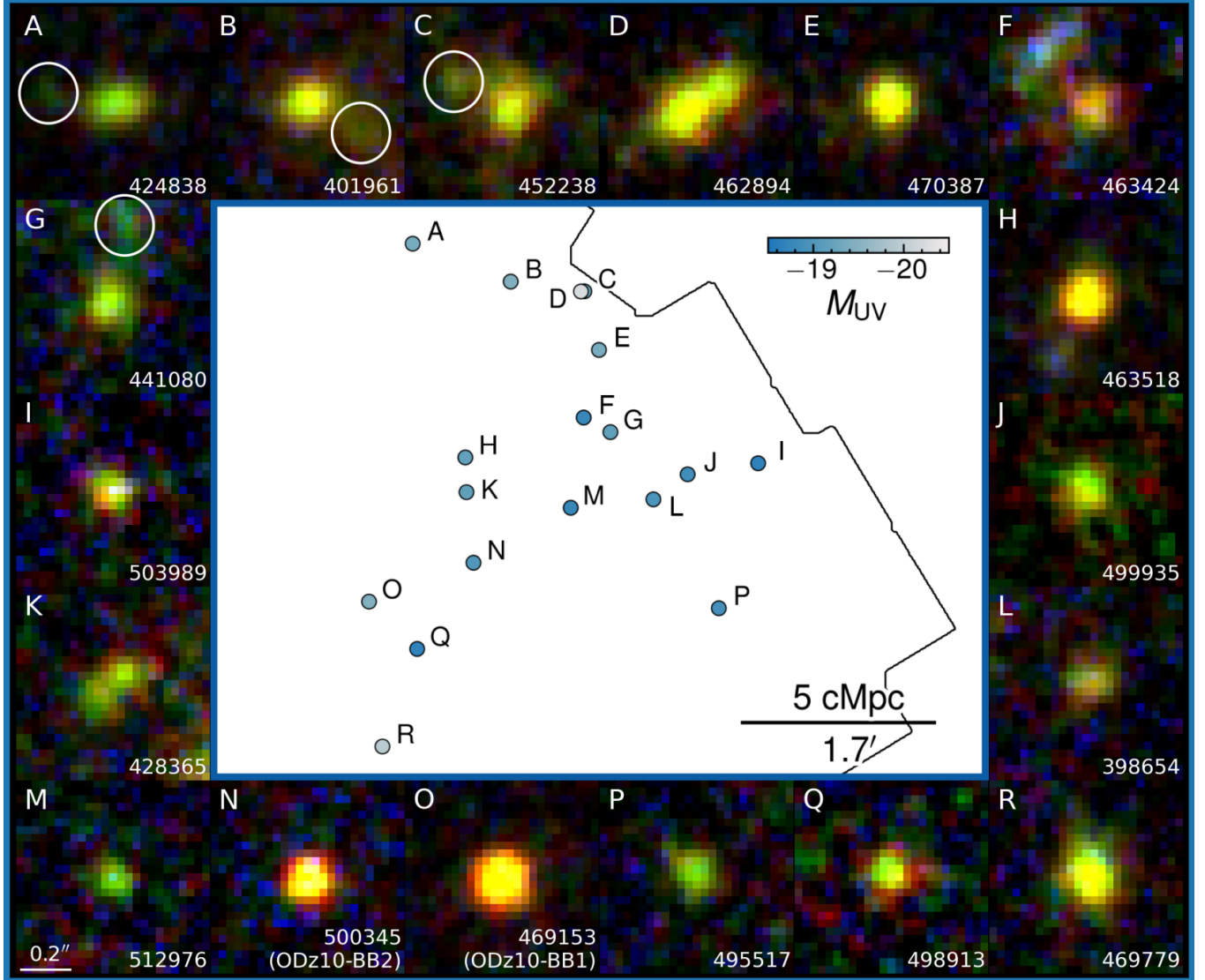


Figure 2. Composite view of the $z \approx 10.5$ overdensity. The central panel shows the relative projected positions of member galaxies, color-coded by rest-frame UV absolute magnitude M_{UV} . The surrounding panels present JWST/NIRCam cutouts, using the F115W, F277W, and F444W bands as blue, green, and red, respectively, with F115W as the dropout band. Each cutout has a size of $0.75'' \times 0.75''$; the scale bar indicates $0.2''$ (0.8 pkpc). The upper left of each cutout shows object labels ordered by declination, in correspondence with the central panel, and the lower right shows their NIRCam IDs. Objects with close companions that are also F115W dropouts are marked by circles. Objects D and K (IDs 462894 and 428363) each consist of two components at consistent photometric redshifts. The blue companion of object F (ID 463424) is at $z_{\text{phot}} = 1.86$ and not associated with the object.

free multiplicative factor between 0 and 1.5 relative to the `CLOUDY` prediction. The fitting results are summarized in Table 1. We further estimate the UV slope β , defined as the power index in $F_\lambda \propto \lambda^\beta$, from the `Prospector` posterior spectra over the rest-frame wavelength range 1340–2600 Å in the spectral windows defined by D. Calzetti et al. (1994). We infer the absolute UV magnitude from the posterior spectra at rest-frame 1500 Å. Our estimates differ slightly from those of K. N. Hainline et al. (submitted) because our photometry includes extended emission from the galaxies and

their subcomponents, and because we adopt a different SED modeling framework. The photometric redshifts inferred with `Prospector` are slightly lower than `EAZY` results due to the difference in Ly α modeling.

3.2. Balmer Break

Two objects in the overdensity, designated ODz10-BB1 and ODz10-BB2 (IDs 469153 and 500345), show potential Balmer breaks (Figure 3). Their F444W fluxes exceed rest-frame UV continua by 62% and 65%, respectively, with $S/N = 28$ and 13 for the excess detec-

Table 1. Properties of member galaxies in the $z \approx 10.5$ overdensity

ID	Component	RA	Dec	M_{UV}	z_{phot}	β	r_{half}	$\log M_{\star}$	SFR_{30}
		(deg)	(deg)	(mag)			(pc)	(M_{\odot})	($M_{\odot} \text{ yr}^{-1}$)
398654	...	52.955667	-27.808922	-19.0	$9.3_{-0.6}^{+1.1}$	$-2.3_{-0.1}^{+0.1}$	188_{-88}^{+41}	$7.9_{-0.5}^{+0.6}$	$2.0_{-1.1}^{+3.9}$
401961	...	52.980418	-27.775546	-19.5	$9.7_{-0.3}^{+0.5}$	$-2.2_{-0.1}^{+0.1}$	240_{-51}^{+51}	$8.6_{-0.3}^{+0.4}$	$8.0_{-4.3}^{+4.6}$
424838	...	52.997421	-27.769738	-19.4	$11.0_{-0.6}^{+0.6}$	$-2.4_{-0.2}^{+0.2}$	187_{-12}^{+12}	$7.9_{-0.5}^{+0.4}$	$2.2_{-1.2}^{+3.0}$
428365	total	52.988090	-27.807818	-19.2	$10.1_{-0.5}^{+0.8}$	$-2.3_{-0.1}^{+0.1}$...	$8.2_{-0.4}^{+0.3}$	$3.6_{-2.3}^{+1.7}$
...	comp1	52.988113	-27.807835	-18.9	$10.8_{-0.7}^{+1.3}$	$-2.4_{-0.3}^{+0.3}$	117_{-31}^{+37}	$7.8_{-0.5}^{+0.5}$	$1.3_{-0.7}^{+1.7}$
...	comp2	52.988082	-27.807808	-18.2	$10.9_{-0.9}^{+1.2}$	$-2.4_{-0.2}^{+0.2}$	96_{-31}^{+31}	$7.3_{-0.3}^{+0.3}$	$0.7_{-0.3}^{+0.5}$
441080	...	52.963122	-27.798615	-19.2	$10.3_{-0.4}^{+0.5}$	$-2.6_{-0.2}^{+0.2}$	96_{-19}^{+19}	$8.1_{-0.3}^{+0.2}$	$3.5_{-1.2}^{+1.1}$
452238	...	52.967645	-27.777034	-19.3	$10.5_{-0.4}^{+0.7}$	$-1.9_{-0.2}^{+0.2}$	140_{-25}^{+25}	$8.5_{-0.5}^{+0.3}$	$8.5_{-5.1}^{+5.4}$
462894	total	52.968239	-27.777062	-20.2	$10.5_{-0.5}^{+0.9}$	$-2.2_{-0.1}^{+0.1}$...	$8.6_{-0.5}^{+0.4}$	$10.6_{-6.3}^{+7.5}$
...	comp1	52.968249	-27.777068	-19.9	$10.4_{-0.5}^{+0.7}$	$-2.3_{-0.3}^{+0.3}$	257_{-19}^{+38}	$8.4_{-0.4}^{+0.3}$	$7.9_{-4.3}^{+4.5}$
...	comp2	52.968202	-27.777041	-19.0	$10.4_{-0.4}^{+0.6}$	$-2.3_{-0.1}^{+0.1}$	153_{-13}^{+25}	$8.3_{-0.4}^{+0.3}$	$3.4_{-2.1}^{+1.6}$
463424	...	52.967760	-27.796385	-18.8	$11.2_{-1.3}^{+0.8}$	$-2.1_{-0.1}^{+0.1}$	149_{-24}^{+24}	$7.6_{-0.2}^{+0.9}$	$1.1_{-0.4}^{+0.6}$
463518	...	52.988288	-27.802503	-19.2	$11.7_{-0.3}^{+0.3}$	$-1.5_{-0.3}^{+0.3}$	91_{-6}^{+6}	$8.2_{-0.2}^{+0.2}$	$5.0_{-1.0}^{+2.2}$
469153	...	53.004990	-27.824597	-19.5	$10.1_{-0.4}^{+0.4}$	$-2.0_{-0.1}^{+0.1}$	76_{-7}^{+7}	$9.2_{-0.1}^{+0.1}$	$0.1_{-0.1}^{+1.2}$
469779	...	53.002664	-27.846805	-19.9	$11.3_{-0.4}^{+0.4}$	$-2.5_{-0.2}^{+0.2}$	160_{-6}^{+6}	$8.5_{-0.3}^{+0.3}$	$7.8_{-2.7}^{+3.3}$
470387	...	52.965106	-27.786018	-19.4	$10.3_{-0.5}^{+0.9}$	$-2.2_{-0.2}^{+0.2}$	108_{-7}^{+7}	$8.4_{-0.4}^{+0.3}$	$5.9_{-2.9}^{+4.0}$
495517	...	52.944313	-27.825610	-18.9	$10.8_{-0.4}^{+0.4}$	$-2.3_{-0.1}^{+0.1}$	121_{-13}^{+13}	$8.3_{-0.3}^{+0.2}$	$3.8_{-2.3}^{+1.8}$
498913	...	52.996646	-27.831849	-18.7	$10.3_{-0.4}^{+0.5}$	$-1.7_{-0.1}^{+0.1}$	62_{-19}^{+19}	$8.7_{-0.4}^{+0.3}$	$9.3_{-6.8}^{+6.0}$
499935	...	52.949725	-27.805090	-18.9	$10.0_{-0.6}^{+0.5}$	$-1.9_{-0.1}^{+0.1}$	166_{-13}^{+13}	$8.5_{-0.6}^{+0.3}$	$5.3_{-4.1}^{+4.6}$
500345	...	52.986872	-27.818640	-19.0	$9.8_{-0.4}^{+0.4}$	$-2.2_{-0.1}^{+0.1}$	9_{-7}^{+7}	$8.7_{-0.2}^{+0.1}$	$3.1_{-2.5}^{+4.1}$
503989	...	52.937501	-27.803392	-18.7	$9.8_{-0.8}^{+1.1}$	$-2.1_{-0.1}^{+0.1}$	94_{-7}^{+7}	$8.0_{-0.5}^{+0.5}$	$2.1_{-1.0}^{+2.2}$
512976	...	52.970003	-27.810213	-18.7	$10.5_{-0.4}^{+0.4}$	$-2.4_{-0.2}^{+0.2}$	21_{-13}^{+13}	$8.0_{-0.2}^{+0.2}$	$2.6_{-0.9}^{+0.8}$

NOTE—Columns are as follows: (1) NIRCam source ID in the JADES DR5 catalog (B. E. Robertson et al. [submitted](#)); (2) structural component (total or individual components identified from `ForcePho` modeling); (3–4) right ascension and declination in the ICRS coordinate system; (5) absolute UV magnitude at rest-frame 1500 Å, M_{UV} ; (6) photometric redshift inferred from `Prospector` SED fitting; (7) UV continuum slope β measured from `Prospector` posterior spectra; (8) half-light radius r_{half} in proper parsecs, derived from multi-band Sérsic fitting with `ForcePho`; (9) stellar mass inferred from `Prospector` assuming a Chabrier IMF; (10) star formation rate averaged over the past 30 Myr.

tion, where the continua are estimated from the mean of F277W and F356W. The excesses are lower limits of the Balmer break strengths because the F444W band may include contribution from wavelengths blueward of the Balmer break.

The excesses are unlikely to be caused by emission lines. At $z > 9$, H β and [O III] $\lambda 4959, 5007$ lines fall outside the F444W band and therefore cannot contribute. The overdensity is securely at $z > 9$, as indicated by the clear Ly α dropout signatures in our deep F115W imaging. The remaining emission lines within F444W, primarily [O II], [Ne III], and Balmer lines, are rarely strong enough to produce the $\sim 65\%$ flux excess, which requires a rest-frame equivalent width of ~ 550 Å. For comparison, the combined equivalent width of all lines

within F444W in GN-z11 is only 219 Å (A. J. Bunker et al. [2023](#)). That said, a $z \lesssim 9$ interpretation cannot be entirely excluded if extreme DLA absorption, requiring neutral-hydrogen column densities of $N_{\text{HI}} > 10^{23} \text{ cm}^{-2}$, suppresses the F115W flux below our detection limit, although such cases are rare (C. A. Mason et al. [2026](#)). This scenario further requires that the two galaxies are not physically associated with the overdensity, since the system as a whole cannot lie at $z < 9$: it would be highly implausible for all 18 member galaxies to have such extreme column densities simultaneously. Finally, these objects cannot be brown dwarfs given their flat SED in the rest-frame UV across wide and medium bands and the non-detection in F115W, distinct from the SEDs of brown dwarfs (K. N. Hainline et al. [2024](#)).

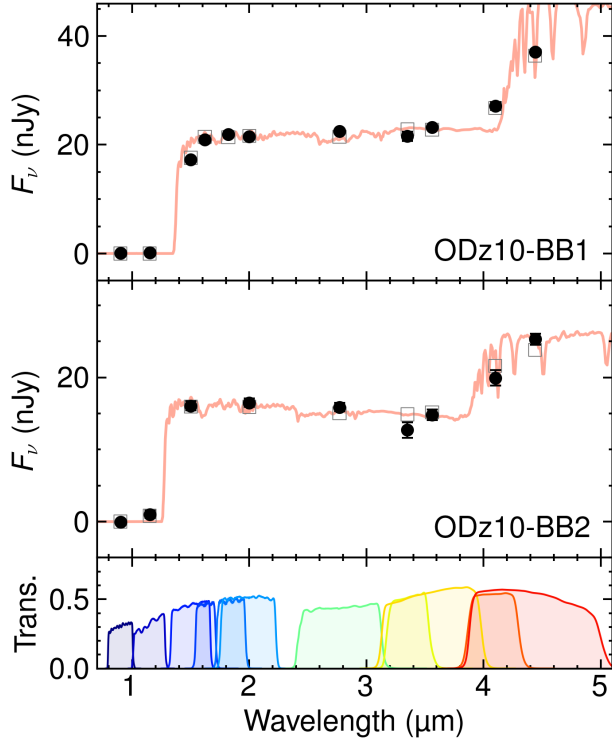


Figure 3. SED of objects with potential Balmer breaks. The upper two panels show NIRCam photometry with error bars (black dots), the best-fit galaxy spectra from `Prospector` (red curves), and synthetic photometry using the best-fit spectra (gray squares). The lower panel shows the transmission curves of NIRCam filters. The Balmer break feature is unlikely to be caused by emission lines, as $\text{H}\beta$ and $[\text{O III}]$ fall outside the F444W band at $z > 9$, while other lines within F444W are rarely strong enough to produce the $\sim 65\%$ flux excess.

Such Balmer breaks, if confirmed, may arise from either the LRD phenomenon (e.g., [J. Matthee et al. 2024](#)) or from an evolved stellar population. The flux increase from F410M to F444W matches the V-shaped SED typical of LRDs ([D. J. Setton et al. 2025](#)). We find their rest-frame optical continuum slopes, β_{optical} (defined as $f_\lambda \propto \lambda^\beta$), are 1.9 ± 0.3 and 1.1 ± 0.7 , derived from power-law fits to the F410M and F444W photometry considering filter throughput. These slopes are characteristic of LRDs ([D. D. Kocevski et al. 2025](#)). Their compact morphologies are also consistent with LRDs: the posterior half-light radii of ODz10-BB1 and ODz10-BB2 are 24 ± 4 and 3 ± 2 mas (96 ± 16 and 12 ± 8 pc), respectively. The point-like morphology of ODz10-BB2 is consistent with known LRDs, and although ODz10-BB1 is slightly extended, it could still be an LRD with a host galaxy that contributes the extended light (e.g., [C.-H. Chen et al. 2025](#); [K. Inayoshi & L. C. Ho 2025](#); [P. Rinaldi et al. 2025](#)).

An evolved stellar population with a Balmer break could also produce the rise in F410M and F444W. Figure 3 shows the best-fit stellar spectra in red curves, where the Balmer break originates from an evolved stellar population. The close match of synthetic photometry (gray squares) with observations indicates that stellar Balmer breaks can explain the F410M and F444W excess. The compact morphologies are also consistent with massive quiescent galaxies at $z \sim 7$ ([A. Weibel et al. 2025a](#)), although such quiescent galaxies are very rare ([W. M. Baker et al. 2025c](#)). This scenario would imply large stellar masses: our SED fitting finds $\log(M_*/M_\odot) = 9.24 \pm 0.12$ and 8.70 ± 0.13 for ODz10-BB1 and ODz10-BB2, respectively. It also implies surprisingly mature stellar populations in the early Universe. We will further discuss the implications in Section 4.1.

3.3. Size–mass Relation

Figure 4b compares the size–mass distribution of galaxies inside the overdensity with field galaxies. The sizes are measured from multiband fitting with `ForcePho` using Sérsic profiles. The primary constraints come from the F150W and F200W bands, probing rest-frame 1130–2000 Å, where the PSFs are the sharpest. We adopt circularized half-light radii r_{half} because the sources are marginally resolved, and the circularized radii are more stable to noise than semi-major radii. For sources with multiple components, we plot the size of the primary component only.

Most galaxies in the overdensity have $r_{\text{half}} \approx 200$ pc, whereas three objects (441080, 512976, and ODz10-BB1) are significantly smaller and consistent with point sources. While ODz10-BB1 has a prominent Balmer break (Section 3.2), 441080 and 512976 are typical young galaxies with blue UV slopes, similar to many other compact star-forming galaxies at high redshifts (e.g., [J. Wittsotk et al. 2025a](#); [Z. Wu et al. 2025](#)). Notably, 441080 has diffuse emission and a companion in the north, but its dominant central component is very compact.

We do not find a significant difference in the size–mass relation compared to field galaxies, although galaxies in the overdensity are slightly more massive. The field sample includes all objects in GOODS-S at similar photometric redshift ($10 < z_{\text{phot}} < 12$) with the same brightness threshold ($F356W > 8$ nJy). We also find consistency in the size distribution with results in [T. Morishita et al. \(2024\)](#) in our mass range. This consistency may suggest that the structural build-up of the galaxies may proceed similarly in dense and average environments at this early epoch.

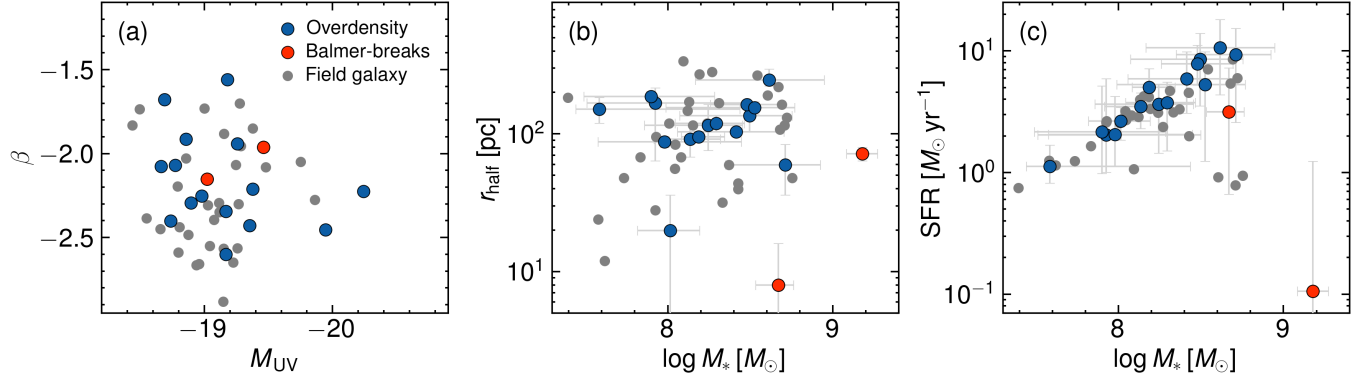


Figure 4. (a) UV continuum slope β versus absolute UV magnitude M_{UV} . (b) Half-light radius versus stellar mass, where sizes are measured from multiband Sérsic fitting using **ForcePho**. (c) Star formation rate averaged over the past 30 Myr versus stellar mass. Blue points denote galaxies in the overdensity, gray points show field galaxies at similar redshifts ($10 < z_{\text{phot}} < 12$) and brightness ($\text{F356W} > 8 \text{ nJy}$), and red points highlight objects in the overdensity with potential Balmer breaks. We assume that the Balmer breaks arise from stellar populations in the SED fitting, although they could alternatively be produced by LRDs.

3.4. Star Formation Rate

Figure 4 shows the star-forming main sequence. SFRs are inferred from **Prospector** fits to the NIRCam SEDs, where we report SFRs averaged over the past 30 Myr, as the rest-frame UV continuum probes SFRs on timescales of 10–50 Myr (R. C. Kennicutt & N. J. Evans 2012). Most galaxies in the overdensity have $\text{SFR} \sim 3 M_{\odot} \text{ yr}^{-1}$ and specific SFR (sSFR) $\sim 40 \text{ Gyr}^{-1}$, implying stellar-mass doubling times of $\sim 25 \text{ Myr}$ if the SFR is sustained.

Galaxies in the overdensity have a median SFR that is $\gtrsim 30\%$ higher than that of the field galaxies at $10 < z_{\text{phot}} < 12$, a difference also reflected in their systematically higher luminosities in Figure 4a. The field sample, shown in Figure 1, is selected with the same criteria ($\text{F356W} > 8 \text{ nJy}$) and measured consistently with **Prospector**. This result suggests enhanced star formation activity in the overdense environment. While studies at $z \approx 5\text{--}7$ find lower SFRs in overdensities relative to the field (J. M. Helton et al. 2024a; Z. Li et al. 2025), our result is consistent with their inference that at earlier epochs, these galaxies should have higher SFRs than field galaxies according to their star formation histories and larger stellar masses (J. M. Helton et al. 2024a).

The total SFR within the overdensity is $98 M_{\odot} \text{ yr}^{-1}$. We estimate a SFR density within the overdensity of $0.05 M_{\odot} \text{ yr}^{-1} \text{ cMpc}^{-3}$, assuming a line-of-sight extent comparable to the transverse scale, and a contribution to the cosmic SFR density of $1.6 \times 10^{-4} M_{\odot} \text{ yr}^{-1} \text{ cMpc}^{-3}$ when averaged over the full GOODS-S field and $\Delta z = 2$. These values should be regarded as lower limits, as faint overdensity members are not included in our selection. The results are slightly higher but broadly consistent with predictions from semi-analytical models of cosmic star formation (e.g., Y.-K. Chiang et al. 2017).

For comparison, the total SFR of field galaxies at $10 < z_{\text{phot}} < 12$ in GOODS-S is $105 M_{\odot} \text{ yr}^{-1}$, implying that the overdensity accounts for $\sim 48\%$ of the total star formation. Simulations predict that proto-clusters account for 50% of cosmic star formation at $z \approx 10$ (Y.-K. Chiang et al. 2017), which is comparable to the fraction inferred for this overdensity. However, this estimate should be interpreted with caution, as our photometric selection may include $\sim 20\%$ contamination from field galaxies projected into the overdensity (Section 2), while additional members may lie outside the current observed footprint, and our analysis is restricted to relatively bright objects. Cosmic variance in GOODS-S may also affect the inferred fractions.

3.5. Galaxy Merger and Clumps

Six galaxies in the overdensity show subcomponents within 1 pkpc that are also F115W dropouts, indicating consistent redshifts. Their NIRCam IDs are 401961, 424838, 428365, 441080, 452238, and 462894. These subcomponents are likely gravitationally bound, as the expected virial radii of their halos are $\sim 8 \text{ pkpc}$, given the stellar-halo mass relation (M. Stefanon et al. 2021).

The subcomponents may originate from galaxy mergers or clumpy star formation. However, the clumpy explanation is less likely because many of these components lie at $\sim 1 \text{ pkpc}$ from the primary component, well beyond the effective radius of the host galaxy. Such offsets are difficult to explain with in-situ stellar clumps.

The fraction of galaxies with subcomponents exceeds that of field galaxies. This fraction is 33% inside the overdensity but is only $\sim 15\%$ among field galaxies based on our visual inspection. For comparison, quantitative analysis of K. N. Hainline et al. (submitted) find 22% galaxies at $z_{\text{phot}} = 10\text{--}11$ show extended emission, which is consistent with our estimate.

The galaxies with subcomponents also show a spatial preference inside the overdensity: five of the six galaxies are located in the northern part of the overdensity. Notably, 452238 and 462894 are separated by only 8.4 pkpc (2.1''). The distance is comparable to the virial radius of their halos and thus may suggest ongoing major mergers. Follow-up spectroscopic observations will be important to confirm their physical association.

3.6. Ly α Emission Estimate

Ideally, Ly α fluxes would be measured directly from spectroscopy (e.g., A. J. Bunker et al. 2023; G. C. Jones et al. 2024, 2025; J. Witstok et al. 2025a). Here, we estimate the flux using our current photometry data, exploiting the fact that Ly α falls within the F150W filter and can boost its flux. Given the photometric uncertainty and the filter bandwidth, the F150W data correspond to a median 1σ ine-flux sensitivity of 2.7×10^{-19} erg s $^{-1}$ cm $^{-2}$, sufficient to detect Ly α with strengths comparable to those of GN-z11 and JADES-GS-z13-0-LA (A. J. Bunker et al. 2023; J. Witstok et al. 2025a). A major limitation, however, is the uncertainties in redshift. The F150W flux is highly sensitive to the precise redshift because it sets the location of the Ly α break, leading to a strong degeneracy between Ly α strength and redshift, which precludes meaningful constraints for individual objects. Nonetheless, this issue is alleviated by the fact that the galaxies lie in the same overdensity and are therefore expected to have similar redshifts. If their line-of-sight separations are comparable to the projected distances (~ 10 cMpc), the implied redshift spread is $\Delta z \simeq 0.05$. Even allowing for large internal velocity offsets, a relative velocity of 1000 km s $^{-1}$ only produces $\Delta z \simeq 0.04$. Both effects are negligible in the context of the F150W bandwidth. By imposing a common redshift for the galaxies, we are therefore able to infer the spatial distribution of Ly α fluxes.

To implement this, we sample a redshift grid from $z = 10.0$ to 11.4 in steps of 0.1. At each grid point, we run `Prospector` SED fits for every galaxy with the redshift held fixed. As in Section 3.1, we fit a Ly α factor, defined as the ratio of the best-fit Ly α flux to the nebular Ly α flux predicted by the `cloudy` model. The modeling includes neutral IGM absorption following P. Madau (1995), with a free scaling parameter that accounts for line-of-sight variations in the total opacity. We adopt a Gaussian prior on this parameter, centered at 1 with a dispersion of 0.3, as the default choice in `Prospector`. The resulting posterior distribution of the Ly α factor has a typical 1σ width of 0.27. We do not model DLA absorption or the effect of ionized bubbles on the IGM, as they are unconstrained in the absence of spectroscopic

data. They are expected to further broaden the uncertainty on the Ly α factor. We qualitatively discuss their potential impact later in this section.

At $z = 10.5$, the redshift favored by the joint posterior of the redshift-free modeling in Section 3.1, the Ly α factor shows a spatial pattern: it is elevated near the center of the overdensity and decreases toward the outskirts (Figure 5b). The radial decrease has a Spearman correlation coefficient of -0.62 ($p = 0.003$, $n = 18$). This behavior is consistent with enhanced Ly α transmission in the core and reduced transmission in the outskirts.

The radial decline is robust across the entire redshift range. For each assumed redshift, we examine the Ly α factor as a function of distance from the overdensity center, where the center is defined as the arithmetic mean of the galaxy coordinates. Although the Ly α factors of individual galaxies vary with redshift, the collective trend is unchanged. Even at $z = 11$, the profile is similar to the $z = 10.5$ case, as shown in Figure 5c. Fitting an exponential profile to the radial variation yields a scale radius of 6 cMpc at $z = 10.5$, and this value remains nearly constant between $z = 10.5$ and 11.

However, the photometric inference is not definitive. First, we assumed all galaxies in the overdensity share the same redshift. Nonetheless, galaxies close in projection could still be widely separated along the line of sight. A configuration in which lower-redshift galaxies lie near the projected center and higher-redshift galaxies on the edge could reproduce the observed pattern. Second, inferring transmission requires an estimate of the intrinsic Ly α flux, which depends on the nebular emission model and the escape fraction of ionizing photons. If galaxies at the edge have higher escape fractions, they would produce lower Ly α flux even under identical IGM transmission. Finally, spatial variations of DLA and IGM absorption may also affect F150W. This effect is complicated: DLA absorption is expected to be enhanced toward the densest regions of the overdensity due to the higher abundance of massive halos along the line of sight, whereas IGM absorption may be enhanced by higher recombination rates or reduced by larger ionized bubbles, depending on the local balance between density and ionizing sources. Direct Ly α and redshift measurements from spectroscopy are therefore essential to test the bubble interpretation.

Finally, we note that the bubble radius inferred from photometric Ly α transmission is consistent with a first-order estimate of the bubble size based on the ionizing photon budget (C. A. Mason & M. Gronke 2020):

$$R_{\text{ion}} \simeq \left(\frac{3 f_{\text{esc}} \dot{N}_{\text{ion}} t_{\text{age}}}{4\pi \bar{n}_{\text{H}}(z)} \right)^{1/3} \gtrsim 4 \text{ cMpc} \quad (1)$$

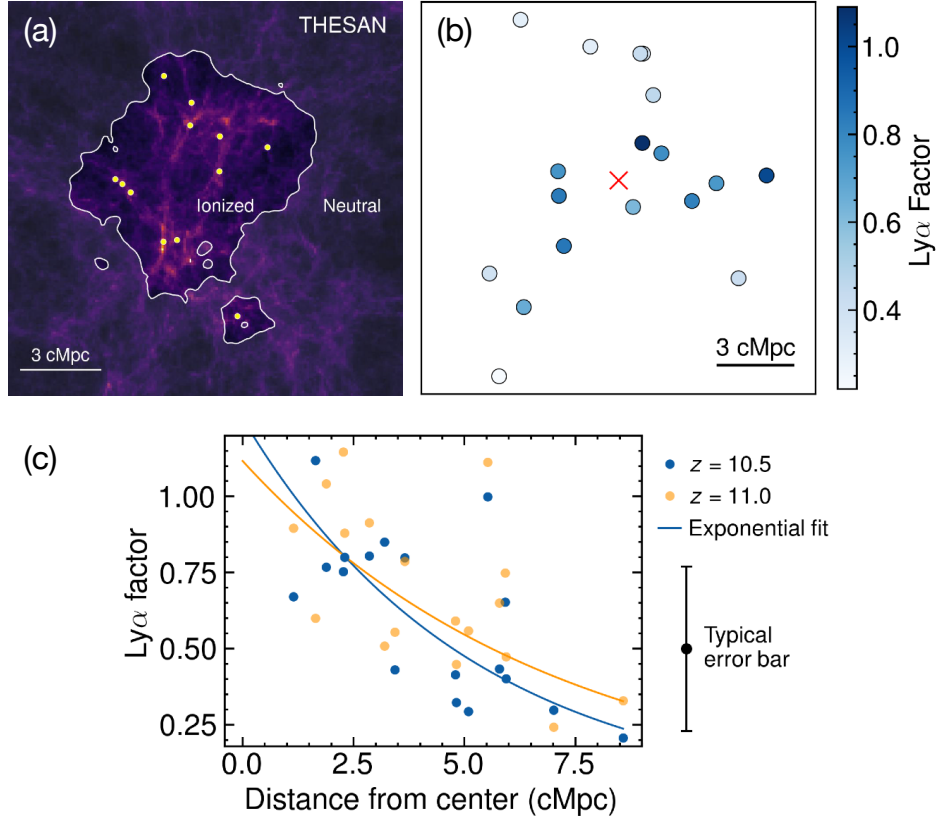


Figure 5. Spatial distribution of Ly α transmission in the overdensity and comparison with simulations. (a) THESAN-1 neutral-hydrogen map around a $z = 10.5$ overdensity, with contours marking regions where the median ionized fraction exceeds 90%. Galaxies with rest-frame U band absolute magnitude brighter than -17.5 mag are shown in yellow. (b) Observed galaxy positions color-coded by their inferred Ly α factor. The Ly α factor quantifies Ly α transmissions as the ratio of inferred Ly α flux to that produced by the galaxies according to nebular models. We estimate them from photometry using `prospector` while fixing the redshift of all galaxies to the median photometric redshift $z = 10.5$. The red cross marks the geometric center of the overdensity. (c) Ly α factor versus comoving radius for two assumed redshifts ($z = 10.5$ and 11.0), showing a robust declining trend despite redshift uncertainties.

where we assume an escape fraction $f_{\text{esc}} = 5\%$ following J. Witstok et al. (2024) and a characteristic duration of ionizing photon production $t_{\text{age}} = 30$ Myr according to the median stellar age from our SED fitting. At the level of this order-of-magnitude estimate, the resulting bubble size depends only weakly on these parameters. We calculate \bar{n}_{H} according to the mean cosmological hydrogen number density at redshift z . The total ionizing photon production rate \dot{N}_{ion} is estimated by summing the contributions from all galaxies within the overdensity, inferred from their M_{UV} and β using the prescription of C. A. Mason & M. Gronke (2020). This estimate should be regarded as a lower limit, as our sample includes only relatively bright galaxies, while faint sources are expected to contribute additional ionizing photons.

4. DISCUSSION

4.1. Implications for Early Galaxy Evolution

The first- and second-most luminous galaxies in the overdensity are 462894 and 469779, respectively, with absolute UV magnitudes of $M_{\text{UV}} = -20.2$ and -19.9 . They are the brightest galaxies across the entire GOODS-S field at $10 < z_{\text{phot}} < 12$. The concentration of the most luminous objects within such a small region indicates that the overdensity hosts a disproportionately large number of the brightest galaxies, providing evidence that overdensities host the most massive halos.

Even so, these galaxies are still fainter than several of the most luminous known sources at $z > 10$, such as GNz11, JADES-GS-z14-0, and GHZ2 (A. J. Bunker et al. 2023; S. Carniani et al. 2024; M. Castellano et al. 2024), whose absolute UV magnitudes are brighter by ~ 1 mag. If the most massive halos reside in overden-

sities, such “over-luminous” galaxies should likewise lie in overdense environments, yet no luminous companions are detected around them. Although GN-z11 has a candidate proto-cluster, its significance is far weaker than the overdensity reported here (S. Tacchella et al. 2023; J. Scholtz et al. 2024). The isolation of “over-luminous” galaxies suggests either that they occupy unusually massive halos even in the field, or that their luminosities are powered by extreme star-formation processes or active galactic nuclei.

Another possibility is that the most massive galaxies in the overdensity are no longer the most UV luminous. Two galaxies in the overdensity show potential Balmer breaks. If these Balmer breaks arise from evolved stellar populations, the implied stellar masses of $\log(M_*/M_\odot) = 9.2$ and 8.6 are consistent with the expected descendants of over-luminous objects like JADES-GS-z14-0, given its star-formation rate. `Prospector` modeling further indicates that these Balmer-break galaxies experienced a peak star-formation rate of $\sim 10 M_\odot \text{ yr}^{-1}$ at $z \approx 12$, which then declined to $\sim 5 \times 10^{-2} M_\odot \text{ yr}^{-1}$, leaving them faint. If confirmed, these objects would provide the missing observational link to the descendants of the overluminous $z > 10$ population and would imply strongly bursty star formation in the early universe (K. Boyett et al. 2024). Similar massive (mini-)quenched galaxies have already been identified in overdensities at $z \approx 5$ (W. M. Baker et al. 2025a).

4.2. Implications for Cosmic Reionization

We find that Ly α transmission may be nearly transparent around the overdensity center and is consistent with declining toward its outskirts. This appears as a decrease in the F150W flux relative to the UV continuum from the center to the edge. We quantify the transmission by fitting the SEDs of all galaxies with their redshifts fixed to a common value over a redshift grid, as described in Section 3.6. The declining trend is robust because it persists across the full redshift range we tested and thus may suggest an ionized bubble forming in the overdensity.

If confirmed, the spatial variation of Ly α transmission would mark the earliest ionized bubble produced by a galaxy overdensity known so far. It provides a rare laboratory to study the structure of ionizing bubbles. Previous Ly α detections from JADES-GS-z13-1-LAE imply bubble sizes of ~ 5 cMpc (J. Witstok et al. 2025a), but these estimates rely on detailed radiative transfer modeling. In contrast, the overdensity enables direct constraints from the spatial distribution of Ly α transmission. Spectroscopic redshifts for galaxies at different

line-of-sight positions would further map variations in Ly α transmission within the bubble. These measurements would place strong constraints on the physics of cosmic reionization in the early universe.

4.3. Comparison with Cosmological Hydrodynamical Simulations

We compare this galaxy population to that of the THESAN simulation. THESAN is a suite of large-volume cosmological radiation-magneto-hydrodynamic simulations of the Epoch of Reionization, combining the IllustrisTNG galaxy-formation framework with a self-consistent treatment of hydrogen reionization (R. Kannan et al. 2022). However, it is well-known that current simulations underpredict the luminosity function of galaxies at $z > 10$ (e.g., S. L. Finkelstein et al. 2023; C. T. Donnan et al. 2024; S. L. Finkelstein et al. 2024; A. Weibel et al. 2025b; L. Whitler et al. 2025).

We do not find a comparable overdensity in the THESAN simulation. We search for overdensities in the fiducial THESAN-1 run, which has a box size of 95.5 cMpc, equivalent to five times the JADES GOODS-S area. We select galaxies using the same flux limit of F356W $> 8 \text{ nJy}$, corresponding to the rest-frame U -band in THESAN. Under this selection, the maximum overdensity within an 8 cMpc radius contains only six galaxies, far fewer than observed. The stellar masses of these galaxies range from $0.5\text{--}2.4 \times 10^8 M_\odot$, with a median of $6 \times 10^7 M_\odot$, which are $\sim 40\%$ lower than the masses of galaxies in our observed overdensity.

However, we do recover comparable overdensities once we brighten the simulated galaxies by 1 mag in an *ad hoc* way. This adjustment also brings the simulated galaxy number density into agreement with JADES. In this case, the most overdense region in THESAN contains 17 galaxies within 5 cMpc, of which 14 galaxies also lie within 5 cMpc in the z -direction, while the remaining three are separated by 30–60 cMpc and appear close only due to projection. This overdensity generates an ionized bubble with ionized hydrogen fractions $> 90\%$, computed using the median over 10 cMpc along the line of sight (z direction). The resulting bubble has a radius of ~ 4 cMpc (Figure 5a). It would likely be larger if the galaxies were truly brighter by 1 mag and produced more ionizing photons. This behavior is consistent with the bubble size inferred for our observed overdensity.

5. SUMMARY AND FUTURE PROSPECTS

We identify an overdensity at $z_{\text{phot}} \approx 10.5$ in the JADES GOODS-S field. It contains 18 objects occupying a region only ~ 10 cMpc across, exceeding the average density by a factor of four. Most members are compact, low-mass, and actively star-forming, consistent

with typical scaling relations. Close companions within 1 pkpc occur more frequently than in the field, suggesting enhanced interaction and merger activity. Two compact sources show potential Balmer breaks, suggesting the presence of LRDs or unexpectedly evolved stellar populations within 500 Myr after the Big Bang. We find tentative evidence for spatial variation in Ly α transmission from the photometric data, consistent with the formation of an ionizing bubble with radius ~ 6 cMpc.

These conclusions are necessarily provisional because they rely on photometry alone. Spectroscopic follow-up is essential to establish secure membership of the overdensity. JWST/NIRSpec spectroscopy will provide precise redshifts, confirm or refute Ly α emission, and determine the origin of the potential Balmer breaks. Measurements of the spatial distribution of Ly α flux would directly examine the presence of an ionized bubble. Because Ly α -breaks and Ly α -lines are affected by DLA effects and resonant scattering, respectively, precise redshift measurements require non-resonant tracers. ALMA observations targeting [O III] 88 μ m emission, or JWST/MIRI LRS observations of [O III] λ 5007 and H α , can provide robust redshift measurements for the brightest members, anchoring the three-dimensional structure of the overdensity. Together, these measurements would transform the photometric evidence into a definitive test of early overdense structure formation and the onset of cosmic reionization.

ACKNOWLEDGMENTS

We thank Anna de Graaff for insightful discussions. This work is based on observations made with the NASA/ESA/CSA James Webb Space Telescope. The data were obtained from the Mikulski Archive for Space Telescopes at the Space Telescope Science Institute, which is operated by the Association of Universities for Research in Astronomy, Inc., under NASA contract NAS 5-03127 for JWST. These observations are associated with programs 1286, 1287, 2514, 3215, 3990, 5997, and 6434. This research made use of the lux supercomputer at UC Santa Cruz which is funded by NSF MRI grant AST 1828315.

DJE, BDJ, KH, JH, ZJ, BER, FS, and CNAW acknowledge support from the NIRCam Science Team contract to the University of Arizona, NAS5-02015. DJE is also supported as a Simons Investigator and by NASA through a grant from the Space Telescope Science Institute, which is operated by the Association of Universities for Research in Astronomy, Inc., under NASA contract NAS5-03127. WMB gratefully acknowledges support from DARK via the DARK fellowship and

research grant (VIL54489) from VILLUM FONDEN. AJB acknowledges funding from the “FirstGalaxies” Advanced Grant from the European Research Council (ERC) under the European Union’s Horizon 2020 research and innovation program (Grant agreement No. 789056). AJC gratefully acknowledges support from the Cosmic Dawn Center through the DAWN Fellowship. The Cosmic Dawn Center (DAWN) is funded by the Danish National Research Foundation under grant No. 140. ECL acknowledges support of an STFC Webb Fellowship (ST/W001438/1). ALD thanks the University of Cambridge Harding Distinguished Postgraduate Scholars Programme and Technology Facilities Council (STFC) Center for Doctoral Training (CDT) in Data intensive science at the University of Cambridge (STFC grant number 2742605) for a PhD studentship. RH acknowledges funding provided by the Johns Hopkins University, Institute for Data Intensive Engineering and Science (IDIES). JMH is also supported by JWST program 3215. TJL gratefully acknowledges support from the Swiss National Science Foundation through a SNSF Mobility Fellowship and from the NASA/JWST Program OASIS (PID 5997). RM acknowledges support by the Science and Technology Facilities Council (STFC), by the ERC through Advanced Grant 695671 “QUENCH”, and by the UKRI Frontier Research grant RISEandFALL. RM also acknowledges funding from a research professorship from the Royal Society. BER also acknowledges support from JWST Program 3215. ST acknowledges support by the Royal Society Research Grant G125142. JAAT acknowledges support from the Simons Foundation and JWST program 3215. Support for program 3215 was provided by NASA through a grant from the Space Telescope Science Institute, which is operated by the Association of Universities for Research in Astronomy, Inc., under NASA contract NAS 5-03127. The research of CCW is supported by NOIRLab, which is managed by the Association of Universities for Research in Astronomy (AURA) under a cooperative agreement with the National Science Foundation. JW gratefully acknowledges support from the Cosmic Dawn Center through the DAWN Fellowship. The Cosmic Dawn Center (DAWN) is funded by the Danish National Research Foundation under grant No. 140.

APPENDIX

A. GALAXY SPECTRAL ENERGY DISTRIBUTION

This appendix presents the photometry and best-fit SEDs of galaxies in the overdensity. The photometry in Table A1 is obtained using **ForcePho**, which simultaneously fits the individual galaxy components with Sérsic profiles. Figure A shows the **Prospector** best-fit SEDs based on the total flux summed over all components.

B. CANDIDATES EXCLUDED FROM THE FIDUCIAL SAMPLE

ID 423134 (RA = 53.011013, Dec = -27.833990) This source has a nominal 1.49 ± 0.45 nJy (3.3σ) F115W flux in the JADES DR5 catalog in aperture photometry. However, the measurement is contaminated by a nearby luminous galaxy at $z_{\text{phot}} = 2.88$. The F115W image shows no compact emission associated with the source. Using aperture photometry with a $0.1''$ radius and subtract a local background estimated from an annulus with inner and outer radii of $0.15''$ and $0.2''$, we measure an F115W flux of 0.4 ± 0.8 nJy. The uncertainty includes the formal pixel-level measurement error within the source aperture, as well as contributions from background fluctuations and the uncertainty in the estimated background level, both quantified using the pixel standard deviation within the background annulus. This non-detection thus may imply a Ly α dropout signature at $z > 10$, making the source a plausible member of the overdensity. Nonetheless, we note that the nearby galaxy happens to have a Balmer break between

F115W and F150W, raising concern that the candidate may be associated with this lower-redshift galaxy. Given this possibility, we exclude this source from our fiducial sample. However, this scenario would require an unusually strong Balmer break to explain the non-detection. Comparing with the nearby galaxy with a flux ratio of F115W/F200W = 0.56, this source has a Bayesian 84% upper limit of F115W($< 84\%$)/F200W = 0.11, assuming a non-negative uniform prior following Eisenstein et al. in prep. Such strong Balmer breaks are rare, especially in faint galaxies.

ID 462180 (RA = 52.963890, Dec = -27.817278) This source is marginally detected in F115W at 2.9σ in **ForcePho** photometry. The emission is on the outskirts of the galaxy, making the reality of the flux uncertain. The object contains four subcomponents with consistent photometric redshifts. The SED modeling with **Prospector** favors a solution at $z \approx 9$ due to the tentative F115W flux. This source has a total stellar mass of $\log(M/M_{\odot}) = 8.7^{+1.4}_{-2.6}$ combining all four components.

ID 470678 (RA = 52.992997, Dec = -27.842358) This source is marginally detected in F115W at 2.7σ in **ForcePho** photometry. The tentative emission is compact and centered on the source, suggesting that it may be real. The SED is unusually red, as shown in Figure B. The inferred UV slope is $\beta = -0.7 \pm 0.2$, significantly redder than that of typical high-redshift galaxies. The SED fitting favors substantial dust attenuation with $A_V = 1.06$ and a large stellar mass of $\log(M/M_{\odot}) = 8.9$. Alternatively, it could be an AGN. This source is detected in MIRI/F770W at 114 ± 32 nJy, consistent with a power-law extrapolation from the rest-frame UV flux.

REFERENCES

Almualla, M., Smith, A., Kannan, R., et al. 2025, arXiv e-prints, arXiv:2512.06085.
<https://arxiv.org/abs/2512.06085>

Baker, W. M., Ito, K., Valentino, F., et al. 2025a, arXiv e-prints, arXiv:2509.09761,
doi: [10.48550/arXiv.2509.09761](https://doi.org/10.48550/arXiv.2509.09761)

Baker, W. M., Tacchella, S., Johnson, B. D., et al. 2025b, *Nature Astronomy*, 9, 141,
doi: [10.1038/s41550-024-02384-8](https://doi.org/10.1038/s41550-024-02384-8)

Baker, W. M., Valentino, F., Lagos, C. d. P., et al. 2025c, *A&A*, 702, A270, doi: [10.1051/0004-6361/202555829](https://doi.org/10.1051/0004-6361/202555829)

Bardeen, J. M., Bond, J. R., Kaiser, N., & Szalay, A. S. 1986, *ApJ*, 304, 15, doi: [10.1086/164143](https://doi.org/10.1086/164143)

Behroozi, P., Wechsler, R. H., Hearn, A. P., & Conroy, C. 2019, *Monthly Notices of the Royal Astronomical Society*, 488, 3143, doi: [10.1093/mnras/stz1182](https://doi.org/10.1093/mnras/stz1182)

Boyett, K., Bunker, A. J., Curtis-Lake, E., et al. 2024, *MNRAS*, 535, 1796, doi: [10.1093/mnras/stae2430](https://doi.org/10.1093/mnras/stae2430)

Brammer, G. B., van Dokkum, P. G., & Coppi, P. 2008, *ApJ*, 686, 1503, doi: [10.1086/591786](https://doi.org/10.1086/591786)

Bunker, A. J., Saxena, A., Cameron, A. J., et al. 2023, *A&A*, 677, A88, doi: [10.1051/0004-6361/202346159](https://doi.org/10.1051/0004-6361/202346159)

Byler, N., Dalcanton, J. J., Conroy, C., & Johnson, B. D. 2017, *ApJ*, 840, 44, doi: [10.3847/1538-4357/aa6c66](https://doi.org/10.3847/1538-4357/aa6c66)

Calzetti, D., Kinney, A. L., & Storchi-Bergmann, T. 1994, *ApJ*, 429, 582, doi: [10.1086/174346](https://doi.org/10.1086/174346)

Table A1. JWST/NIRCam photometry for galaxies in the overdensity.

ID	Component	F090W	F115W	F150W	F162M	F182M	F200W	F210M	F250M	F277W	F300M	F335M	F356W	F410M	F444W		
		(nJy)															
398654	...	0.1 ± 1.1	1.6 ± 1.1	15.8 ± 0.9	16.5 ± 1.8	17.4 ± 1.4	14.6 ± 1.3	12.2 ± 1.3	18.8 ± 2.8	13.8 ± 1.1	15.9 ± 1.7	11.8 ± 1.6	16.9 ± 1.0	15.1 ± 2.0	17.7 ± 1.5		
401961	total	0.7 ± 0.8	-0.6 ± 0.8	21.4 ± 1.3	...	22.6 ± 1.7	22.3 ± 1.5	21.5 ± 1.3	17.2 ± 1.3	21.0 ± 0.9	24.5 ± 1.1	22.0 ± 0.8	24.5 ± 1.1	22.3 ± 1.0	
401961	comp_1	0.7 ± 0.7	-0.2 ± 0.7	17.7 ± 0.7	...	22.0 ± 0.6	18.6 ± 0.5	19.8 ± 1.2	15.9 ± 1.1	17.3 ± 0.5	22.3 ± 1.0	19.6 ± 0.7	22.3 ± 1.0	19.6 ± 0.7	
401961	comp_2	0.0 ± 0.4	-0.3 ± 0.3	3.7 ± 1.0	...	0.6 ± 1.6	3.7 ± 1.5	1.8 ± 0.7	1.2 ± 0.7	3.6 ± 0.8	2.3 ± 0.6	2.4 ± 0.5	2.3 ± 0.6	2.4 ± 0.5	
424838	total	-0.6 ± 0.5	0.3 ± 0.5	14.6 ± 0.5	17.7 ± 1.2	19.9 ± 1.0	18.8 ± 0.5	16.8 ± 0.5	15.5 ± 1.2	14.4 ± 0.5	15.8 ± 1.1	13.1 ± 0.8	13.1 ± 0.8	13.1 ± 0.8	13.1 ± 0.8
424838	comp_1	-0.1 ± 0.5	0.3 ± 0.4	13.5 ± 0.4	17.1 ± 1.1	18.0 ± 0.9	17.4 ± 0.4	15.0 ± 0.4	14.0 ± 1.0	13.2 ± 0.4	14.3 ± 0.9	12.2 ± 0.6	12.2 ± 0.6	12.2 ± 0.6	12.2 ± 0.6
424838	comp_2	-0.4 ± 0.2	0.0 ± 0.2	1.2 ± 0.2	0.6 ± 0.5	1.9 ± 0.4	1.4 ± 0.2	1.8 ± 0.3	1.5 ± 0.7	1.2 ± 0.3	1.5 ± 0.6	0.8 ± 0.5	0.8 ± 0.5	0.8 ± 0.5	0.8 ± 0.5
428365	total	0.3 ± 0.6	-1.6 ± 0.8	15.9 ± 0.9	...	15.8 ± 0.9	13.1 ± 1.1	...	14.1 ± 2.2	11.0 ± 1.3	9.9 ± 2.2	11.8 ± 1.5	11.8 ± 1.5	11.8 ± 1.5	
428365	comp_1	0.1 ± 0.4	-0.7 ± 0.6	7.9 ± 0.6	...	10.0 ± 0.7	7.7 ± 0.8	...	7.1 ± 1.6	6.1 ± 1.0	9.1 ± 1.1	9.1 ± 1.1	9.1 ± 1.1	9.1 ± 1.1	
428365	comp_2	0.2 ± 0.5	-0.9 ± 0.6	8.0 ± 0.7	...	5.8 ± 0.6	5.4 ± 0.8	...	7.1 ± 1.5	4.9 ± 0.9	3.8 ± 1.5	2.7 ± 1.0	2.7 ± 1.0	2.7 ± 1.0	
441080	total	-0.8 ± 0.9	0.7 ± 0.9	20.9 ± 0.9	...	22.3 ± 1.0	18.6 ± 0.9	...	17.5 ± 1.7	17.6 ± 1.0	16.4 ± 1.6	15.2 ± 1.2	15.2 ± 1.2	15.2 ± 1.2	
441080	comp_1	0.6 ± 0.6	0.1 ± 0.6	13.8 ± 0.6	...	15.6 ± 0.7	12.8 ± 0.6	...	9.9 ± 1.1	10.9 ± 0.7	10.9 ± 1.1	11.9 ± 0.9	11.9 ± 0.9	11.9 ± 0.9	
441080	comp_2	-1.4 ± 0.7	0.7 ± 0.7	7.1 ± 0.7	...	6.7 ± 0.8	5.8 ± 0.7	...	7.6 ± 1.3	6.7 ± 0.8	5.5 ± 1.2	3.3 ± 0.9	3.3 ± 0.9	3.3 ± 0.9	
452238	total	-1.2 ± 0.9	1.3 ± 0.7	17.2 ± 0.8	22.3 ± 1.4	23.5 ± 1.1	24.0 ± 0.8	22.7 ± 0.8	19.4 ± 1.5	22.7 ± 1.3	20.7 ± 0.7	26.9 ± 1.5	25.7 ± 1.0	25.7 ± 1.0	25.7 ± 1.0
452238	comp_1	-1.0 ± 0.7	0.8 ± 0.6	11.9 ± 0.6	17.5 ± 1.2	16.6 ± 0.9	18.0 ± 0.7	17.9 ± 0.7	14.6 ± 1.3	18.7 ± 1.0	16.3 ± 0.6	22.3 ± 1.1	20.9 ± 0.8	20.9 ± 0.8	20.9 ± 0.8
452238	comp_2	-0.2 ± 0.5	0.5 ± 0.4	5.3 ± 0.5	4.8 ± 0.8	6.9 ± 0.6	6.0 ± 0.5	4.8 ± 0.5	4.7 ± 0.8	4.0 ± 0.8	4.5 ± 0.4	4.6 ± 0.9	4.8 ± 0.6	4.8 ± 0.6	4.8 ± 0.6
462180	total	-2.0 ± 1.1	3.1 ± 1.1	34.7 ± 1.0	41.6 ± 1.9	36.4 ± 1.5	33.5 ± 1.3	28.8 ± 1.4	31.7 ± 2.9	31.2 ± 1.3	26.4 ± 2.1	26.7 ± 1.8	28.7 ± 1.2	27.9 ± 2.4	32.4 ± 1.8	32.4 ± 1.8	
462180	comp_1	-0.9 ± 0.8	1.8 ± 0.7	19.0 ± 0.6	23.2 ± 1.3	19.7 ± 1.0	18.3 ± 0.9	16.4 ± 0.9	16.9 ± 1.7	15.3 ± 0.8	13.6 ± 1.3	13.6 ± 1.0	15.6 ± 0.7	16.4 ± 1.4	17.3 ± 1.0	17.3 ± 1.0	
462180	comp_2	0.0 ± 0.5	0.4 ± 0.5	9.5 ± 0.4	9.4 ± 0.9	9.6 ± 0.7	8.1 ± 0.6	6.6 ± 0.7	7.5 ± 1.4	7.9 ± 0.6	6.3 ± 1.1	6.3 ± 0.9	6.3 ± 0.6	8.1 ± 1.2	7.7 ± 0.9	7.7 ± 0.9	
462180	comp_3	0.3 ± 0.4	0.1 ± 0.4	3.7 ± 0.3	4.0 ± 0.7	3.6 ± 0.6	3.6 ± 0.5	2.9 ± 0.6	3.1 ± 1.2	3.8 ± 0.5	3.5 ± 0.8	3.9 ± 0.8	3.8 ± 0.5	2.3 ± 1.1	4.5 ± 0.8	4.5 ± 0.8	
462180	comp_4	-1.4 ± 0.5	0.8 ± 0.5	2.5 ± 0.4	5.0 ± 0.9	3.4 ± 0.7	3.0 ± 0.6	3.0 ± 0.6	4.2 ± 1.4	4.2 ± 0.6	3.0 ± 0.9	2.8 ± 0.9	3.0 ± 0.6	1.1 ± 1.2	2.9 ± 0.9	2.9 ± 0.9	
462894	total	1.7 ± 0.9	-0.5 ± 0.7	35.4 ± 0.8	41.0 ± 1.5	41.3 ± 1.2	44.0 ± 0.9	36.7 ± 1.0	31.2 ± 3.5	33.4 ± 1.5	34.6 ± 0.8	38.8 ± 1.7	37.2 ± 1.1	37.2 ± 1.1	
462894	comp_1	1.6 ± 0.7	-0.7 ± 0.5	25.1 ± 0.7	28.5 ± 1.2	29.8 ± 1.0	30.7 ± 0.7	26.1 ± 0.8	23.0 ± 3.2	23.2 ± 1.2	25.3 ± 0.7	29.7 ± 1.3	25.6 ± 0.9	25.6 ± 0.9	
462894	comp_2	0.1 ± 0.6	0.2 ± 0.4	10.3 ± 0.5	12.5 ± 0.9	11.6 ± 0.7	13.4 ± 0.5	10.6 ± 0.6	8.2 ± 1.2	10.2 ± 0.9	9.4 ± 0.5	9.1 ± 1.0	11.6 ± 0.7	11.6 ± 0.7	
463424	...	0.2 ± 0.7	1.4 ± 0.7	9.4 ± 0.7	...	10.1 ± 0.7	9.0 ± 0.6	...	8.4 ± 1.2	9.5 ± 0.8	10.0 ± 1.2	16.0 ± 0.9	16.0 ± 0.9	16.0 ± 0.9	
463518	...	0.0 ± 0.3	0.0 ± 0.3	16.9 ± 0.4	23.2 ± 0.7	15.7 ± 0.6	16.2 ± 0.4	16.9 ± 0.5	17.6 ± 2.6	23.4 ± 0.8	22.7 ± 0.4	26.0 ± 0.8	23.5 ± 0.6	23.5 ± 0.6	
469153	...	0.1 ± 0.3	0.1 ± 0.2	17.3 ± 0.3	21.0 ± 0.6	21.9 ± 0.6	21.5 ± 0.3	22.5 ± 0.4	18.2 ± 3.2	21.6 ± 0.8	23.2 ± 0.4	27.1 ± 0.7	37.0 ± 0.5	37.0 ± 0.5	
469779	...	0.7 ± 0.6	-0.1 ± 0.6	13.8 ± 0.6	28.6 ± 1.2	29.6 ± 0.9	28.3 ± 0.4	27.5 ± 0.9	28.4 ± 1.7	24.4 ± 0.8	19.1 ± 2.5	22.4 ± 1.1	20.8 ± 0.7	21.3 ± 1.4	22.9 ± 1.1	22.9 ± 1.1	
470387	...	-0.2 ± 0.4	0.2 ± 0.3	16.3 ± 0.4	18.9 ± 0.7	20.8 ± 0.6	19.4 ± 0.4	17.4 ± 0.4	13.6 ± 2.3	16.5 ± 0.8	16.1 ± 0.5	18.9 ± 0.8	18.6 ± 0.6	18.6 ± 0.6	
470678	...	0.2 ± 0.5	2.3 ± 0.5	7.3 ± 0.5	...	8.3 ± 0.6	...	10.3 ± 1.3	11.1 ± 0.8	11.2 ± 1.5	15.2 ± 1.0	16.3 ± 0.6	21.1 ± 1.4	44.9 ± 1.1	44.9 ± 1.1		
495517	...	-0.7 ± 0.6	-0.2 ± 0.6	7.5 ± 0.5	12.5 ± 0.8	11.0 ± 0.7	12.0 ± 0.7	10.5 ± 0.6	11.1 ± 1.4	9.9 ± 0.6	9.5 ± 0.9	9.2 ± 0.9	9.6 ± 0.5	9.2 ± 1.1	8.6 ± 0.9	8.6 ± 0.9	
498913	...	-1.2 ± 0.4	0.3 ± 0.4	8.5 ± 0.5	10.3 ± 1.0	12.3 ± 0.8	10.3 ± 1.1	11.3 ± 0.8	12.6 ± 1.2	11.8 ± 0.5	11.4 ± 1.2	12.4 ± 1.0	13.0 ± 0.7	13.7 ± 1.1	14.1 ± 1.3	14.1 ± 1.3	
499935	11.5 ± 1.0	12.0 ± 1.0	13.4 ± 0.8	...	12.1 ± 0.8	15.3 ± 1.5	13.5 ± 0.9	13.2 ± 1.3	13.0 ± 1.0	12.6 ± 0.7	12.2 ± 1.7	13.4 ± 1.3	13.4 ± 1.3		
500345	...	-0.1 ± 0.3	1.0 ± 0.5	16.1 ± 0.6	...	16.5 ± 0.6	15.9 ± 0.6	...	12.7 ± 1.1	14.8 ± 0.7	19.9 ± 1.1	25.3 ± 0.8	25.3 ± 0.8		
503989	...	1.2 ± 0.7	1.2 ± 0.7	11.2 ± 0.6	10.9 ± 0.8	10.6 ± 0.7	8.7 ± 0.8	10.6 ± 0.6	11.5 ± 1.3	9.7 ± 0.8	9.5 ± 1.2	9.6 ± 0.9	11.3 ± 0.7	9.9 ± 1.5	13.3 ± 1.2	13.3 ± 1.2	
512976	...	0.1 ± 0.4	0.5 ± 0.4	8.5 ± 0.4	11.0 ± 0.7	10.4 ± 0.6	9.4 ± 0.6	9.8 ± 1.2	7.6 ± 0.7	8.1 ± 0.8	7.1 ± 0.9	8.1 ± 0.6	5.7 ± 1.4	5.7 ± 1.1	5.7 ± 1.1		

Note—Fluxes are derived from `ForcePho` fitting with Sersic profiles across all available NIRCam bands. For galaxies with multiple structural components, fluxes for each component are listed separately.

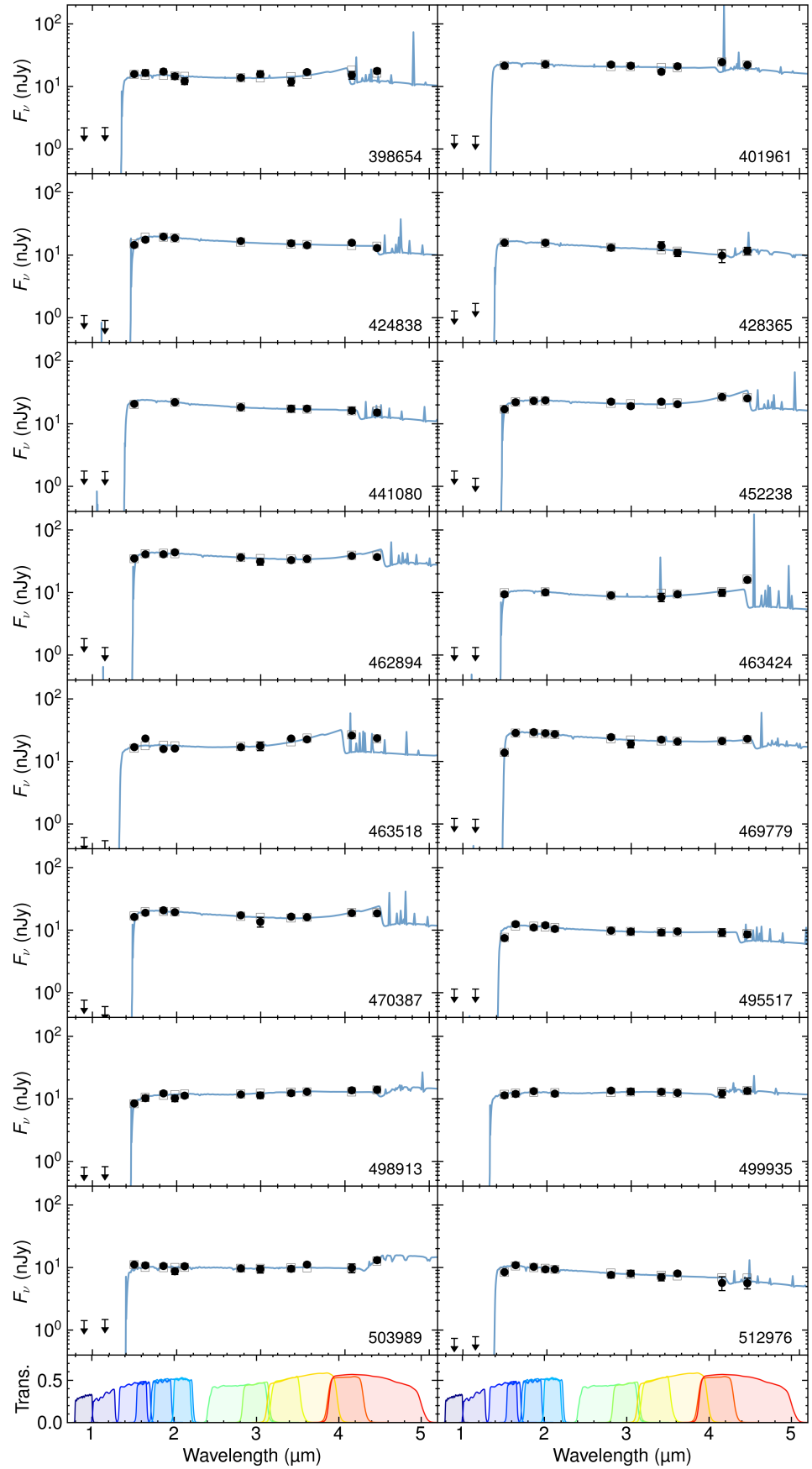


Figure A. SEDs of the other objects in the overdensity, similar to Figure 3. Non-detections are shown as 2σ upper limits.

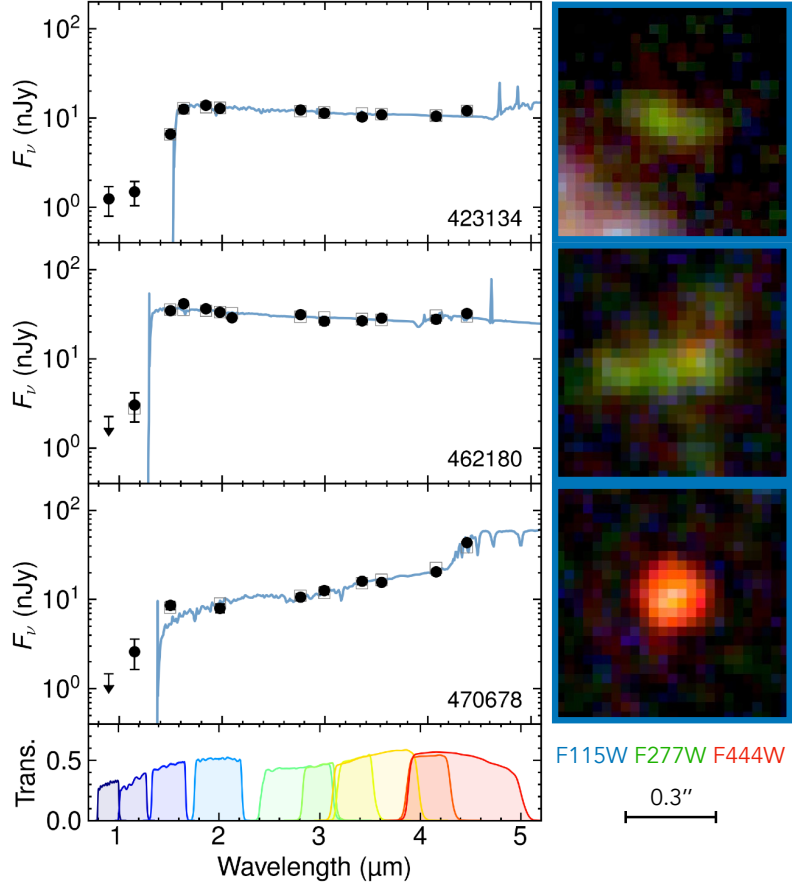


Figure B. SEDs and cutout images of three objects that are excluded from the fiducial sample.

Carniani, S., Hainline, K., D'Eugenio, F., et al. 2024, *Nature*, 633, 318, doi: [10.1038/s41586-024-07860-9](https://doi.org/10.1038/s41586-024-07860-9)

Castellano, M., Dayal, P., Pentericci, L., et al. 2016, *ApJL*, 818, L3, doi: [10.3847/2041-8205/818/1/L3](https://doi.org/10.3847/2041-8205/818/1/L3)

Castellano, M., Napolitano, L., Fontana, A., et al. 2024, *The Astrophysical Journal*, 972, 143, doi: [10.3847/1538-4357/ad5f88](https://doi.org/10.3847/1538-4357/ad5f88)

Castellano, M., Napolitano, L., Fontana, A., et al. 2024, *ApJ*, 972, 143, doi: [10.3847/1538-4357/ad5f88](https://doi.org/10.3847/1538-4357/ad5f88)

Chabrier, G. 2003, *PASP*, 115, 763, doi: [10.1086/376392](https://doi.org/10.1086/376392)

Chen, C.-H., Ho, L. C., Li, R., & Zhuang, M.-Y. 2025, *ApJ*, 983, 60, doi: [10.3847/1538-4357/ada93a](https://doi.org/10.3847/1538-4357/ada93a)

Chen, Z., Stark, D. P., Mason, C. A., et al. 2025, arXiv e-prints, arXiv:2505.24080, doi: [10.48550/arXiv.2505.24080](https://doi.org/10.48550/arXiv.2505.24080)

Chiang, Y.-K., Overzier, R. A., Gebhardt, K., & Henriques, B. 2017, *ApJL*, 844, L23, doi: [10.3847/2041-8213/aa7e7b](https://doi.org/10.3847/2041-8213/aa7e7b)

Choi, J., Dotter, A., Conroy, C., et al. 2016, *ApJ*, 823, 102, doi: [10.3847/0004-637X/823/2/102](https://doi.org/10.3847/0004-637X/823/2/102)

Conroy, C. 2013, *ARA&A*, 51, 393, doi: [10.1146/annurev-astro-082812-141017](https://doi.org/10.1146/annurev-astro-082812-141017)

Conroy, C., Gunn, J. E., & White, M. 2009, *ApJ*, 699, 486, doi: [10.1088/0004-637X/699/1/486](https://doi.org/10.1088/0004-637X/699/1/486)

Curtis-Lake, E., Carniani, S., Cameron, A., et al. 2023, *Nature Astronomy*, 7, 622, doi: [10.1038/s41550-023-01918-w](https://doi.org/10.1038/s41550-023-01918-w)

Donnan, C. T., McLure, R. J., Dunlop, J. S., et al. 2024, *MNRAS*, 533, 3222, doi: [10.1093/mnras/stae2037](https://doi.org/10.1093/mnras/stae2037)

Eisenstein, D. J., Willott, C., Alberts, S., et al. 2023, arXiv e-prints, arXiv:2306.02465, doi: [10.48550/arXiv.2306.02465](https://doi.org/10.48550/arXiv.2306.02465)

Eisenstein, D. J., Johnson, B. D., Robertson, B., et al. 2025, *ApJS*, 281, 50, doi: [10.3847/1538-4365/ae1137](https://doi.org/10.3847/1538-4365/ae1137)

Endsley, R., & Stark, D. P. 2022, *MNRAS*, 511, 6042, doi: [10.1093/mnras/stac524](https://doi.org/10.1093/mnras/stac524)

Finkelstein, S. L., Bagley, M. B., Ferguson, H. C., et al. 2023, *ApJL*, 946, L13, doi: [10.3847/2041-8213/acade4](https://doi.org/10.3847/2041-8213/acade4)

Finkelstein, S. L., Leung, G. C. K., Bagley, M. B., et al. 2024, *ApJL*, 969, L2, doi: [10.3847/2041-8213/ad4495](https://doi.org/10.3847/2041-8213/ad4495)

Fudamoto, Y., Nakazato, Y., Ceverino, D., et al. 2025a, arXiv e-prints, arXiv:2510.11770, doi: [10.48550/arXiv.2510.11770](https://doi.org/10.48550/arXiv.2510.11770)

Fudamoto, Y., Helton, J. M., Lin, X., et al. 2025b, arXiv e-prints, arXiv:2503.15597, doi: [10.48550/arXiv.2503.15597](https://doi.org/10.48550/arXiv.2503.15597)

Furlanetto, S. R., Zaldarriaga, M., & Hernquist, L. 2004, ApJ, 613, 1, doi: [10.1086/423025](https://doi.org/10.1086/423025)

Hainline, K. N., Helton, J. M., Johnson, B. D., et al. 2024, ApJ, 964, 66, doi: [10.3847/1538-4357/ad20d1](https://doi.org/10.3847/1538-4357/ad20d1)

Hainline, K. N., Eisenstein, D. J., Whitler, L., et al. submitted, ApJ

Hashimoto, T., Álvarez-Márquez, J., Fudamoto, Y., et al. 2023, ApJL, 955, L2, doi: [10.3847/2041-8213/acf57c](https://doi.org/10.3847/2041-8213/acf57c)

Helton, J. M., Sun, F., Woodrum, C., et al. 2024a, ApJ, 962, 124, doi: [10.3847/1538-4357/ad0da7](https://doi.org/10.3847/1538-4357/ad0da7)

Helton, J. M., Sun, F., Woodrum, C., et al. 2024b, ApJ, 974, 41, doi: [10.3847/1538-4357/ad6867](https://doi.org/10.3847/1538-4357/ad6867)

Hu, W., Wang, J., Infante, L., et al. 2021, Nature Astronomy, 5, 485, doi: [10.1038/s41550-020-01291-y](https://doi.org/10.1038/s41550-020-01291-y)

Iliev, I. T., Mellema, G., Pen, U.-L., et al. 2006, Monthly Notices of the Royal Astronomical Society, 369, 1625, doi: [10.1111/j.1365-2966.2006.10502.x](https://doi.org/10.1111/j.1365-2966.2006.10502.x)

Inayoshi, K., & Ho, L. C. 2025, arXiv e-prints, arXiv:2512.03130, doi: [10.48550/arXiv.2512.03130](https://doi.org/10.48550/arXiv.2512.03130)

Ishigaki, M., Ouchi, M., & Harikane, Y. 2016, ApJ, 822, 5, doi: [10.3847/0004-637X/822/1/5](https://doi.org/10.3847/0004-637X/822/1/5)

Johnson, B. D., Leja, J., Conroy, C., & Speagle, J. S. 2021, ApJS, 254, 22, doi: [10.3847/1538-4365/abef67](https://doi.org/10.3847/1538-4365/abef67)

Johnson, B. D., Robertson, B. E., Eisenstein, D. J., et al. submitted, ApJ

Jones, G. C., Bunker, A. J., Saxena, A., et al. 2024, A&A, 683, A238, doi: [10.1051/0004-6361/202347099](https://doi.org/10.1051/0004-6361/202347099)

Jones, G. C., Bunker, A. J., Saxena, A., et al. 2025, MNRAS, 536, 2355, doi: [10.1093/mnras/stae2670](https://doi.org/10.1093/mnras/stae2670)

Kannan, R., Smith, A., Garaldi, E., et al. 2022, Monthly Notices of the Royal Astronomical Society, 514, 3857, doi: [10.1093/mnras/stac1557](https://doi.org/10.1093/mnras/stac1557)

Kennicutt, R. C., & Evans, N. J. 2012, ARA&A, 50, 531, doi: [10.1146/annurev-astro-081811-125610](https://doi.org/10.1146/annurev-astro-081811-125610)

Kocevski, D. D., Finkelstein, S. L., Barro, G., et al. 2025, ApJ, 986, 126, doi: [10.3847/1538-4357/adbc7d](https://doi.org/10.3847/1538-4357/adbc7d)

Kravtsov, A. V., & Borgani, S. 2012, ARA&A, 50, 353, doi: [10.1146/annurev-astro-081811-125502](https://doi.org/10.1146/annurev-astro-081811-125502)

Kriek, M., & Conroy, C. 2013, ApJL, 775, L16, doi: [10.1088/2041-8205/775/1/L16](https://doi.org/10.1088/2041-8205/775/1/L16)

Kulkarni, G., & Choudhury, T. R. 2011, Monthly Notices of the Royal Astronomical Society, 412, 2781, doi: [10.1111/j.1365-2966.2010.18100.x](https://doi.org/10.1111/j.1365-2966.2010.18100.x)

Laporte, N., Zitrin, A., Dole, H., et al. 2022, A&A, 667, L3, doi: [10.1051/0004-6361/202244719](https://doi.org/10.1051/0004-6361/202244719)

Larson, R. L., Finkelstein, S. L., Hutchison, T. A., et al. 2022, ApJ, 930, 104, doi: [10.3847/1538-4357/ac5dbd](https://doi.org/10.3847/1538-4357/ac5dbd)

Leonova, E., Oesch, P. A., Qin, Y., et al. 2022, MNRAS, 515, 5790, doi: [10.1093/mnras/stac1908](https://doi.org/10.1093/mnras/stac1908)

Li, Q., Conselice, C. J., Austin, D., et al. 2025a, arXiv e-prints, arXiv:2508.08037, doi: [10.48550/arXiv.2508.08037](https://doi.org/10.48550/arXiv.2508.08037)

Li, Q., Conselice, C. J., Sarron, F., et al. 2025b, MNRAS, 539, 1796, doi: [10.1093/mnras/staf543](https://doi.org/10.1093/mnras/staf543)

Li, Z., Wang, X., Cai, Z., et al. 2022, ApJL, 929, L8, doi: [10.3847/2041-8213/ac626f](https://doi.org/10.3847/2041-8213/ac626f)

Li, Z., Kakiuchi, K., Christensen, L., et al. 2025, A&A, 703, A106, doi: [10.1051/0004-6361/202555372](https://doi.org/10.1051/0004-6361/202555372)

Lim, S., Tacchella, S., Schaye, J., et al. 2024, MNRAS, 532, 4551, doi: [10.1093/mnras/stae1790](https://doi.org/10.1093/mnras/stae1790)

Lu, T.-Y., Mason, C. A., Hutter, A., et al. 2024, MNRAS, 528, 4872, doi: [10.1093/mnras/stae266](https://doi.org/10.1093/mnras/stae266)

Madau, P. 1995, ApJ, 441, 18, doi: [10.1086/175332](https://doi.org/10.1086/175332)

Mason, C. A., Chen, Zuyi, Stark, Daniel P., et al. 2026, A&A, 705, A114, doi: [10.1051/0004-6361/202553820](https://doi.org/10.1051/0004-6361/202553820)

Mason, C. A., & Gronke, M. 2020, MNRAS, 499, 1395, doi: [10.1093/mnras/staa2910](https://doi.org/10.1093/mnras/staa2910)

Matthee, J., Naidu, R. P., Brammer, G., et al. 2024, ApJ, 963, 129, doi: [10.3847/1538-4357/ad2345](https://doi.org/10.3847/1538-4357/ad2345)

McLeod, D. J., Donnan, C. T., McLure, R. J., et al. 2024, MNRAS, 527, 5004, doi: [10.1093/mnras/stad3471](https://doi.org/10.1093/mnras/stad3471)

Mesinger, A., & Furlanetto, S. 2007, ApJ, 669, 663, doi: [10.1086/521806](https://doi.org/10.1086/521806)

Mintz, A., Setton, D. J., Greene, J. E., et al. 2025, arXiv e-prints, arXiv:2506.16510, doi: [10.48550/arXiv.2506.16510](https://doi.org/10.48550/arXiv.2506.16510)

Morishita, T., Roberts-Borsani, G., Treu, T., et al. 2023, ApJL, 947, L24, doi: [10.3847/2041-8213/acb99e](https://doi.org/10.3847/2041-8213/acb99e)

Morishita, T., Stiavelli, M., Chary, R.-R., et al. 2024, ApJ, 963, 9, doi: [10.3847/1538-4357/ad1404](https://doi.org/10.3847/1538-4357/ad1404)

Morishita, T., Liu, Z., Stiavelli, M., et al. 2025a, ApJ, 982, 153, doi: [10.3847/1538-4357/adb30f](https://doi.org/10.3847/1538-4357/adb30f)

Morishita, T., Stiavelli, M., Vanzella, E., et al. 2025b, ApJ, 985, 83, doi: [10.3847/1538-4357/adc4c3](https://doi.org/10.3847/1538-4357/adc4c3)

Morishita, T., Mason, C. A., Kreilgaard, K. C., et al. 2025c, ApJ, 983, 152, doi: [10.3847/1538-4357/adbbdc](https://doi.org/10.3847/1538-4357/adbbdc)

Naidu, R. P., Oesch, P. A., Brammer, G., et al. 2025 arXiv, doi: [10.48550/arXiv.2505.11263](https://doi.org/10.48550/arXiv.2505.11263)

Neyer, M., Smith, A., Kannan, R., et al. 2024, MNRAS, 531, 2943, doi: [10.1093/mnras/stae1325](https://doi.org/10.1093/mnras/stae1325)

Overzier, R. A. 2016, The Astronomy and Astrophysics Review, 24, 14, doi: [10.1007/s00159-016-0100-3](https://doi.org/10.1007/s00159-016-0100-3)

Perrin, M. D., Sivaramakrishnan, A., Lajoie, C.-P., et al. 2014, in Society of Photo-Optical Instrumentation Engineers (SPIE) Conference Series, Vol. 9143, Space Telescopes and Instrumentation 2014: Optical, Infrared, and Millimeter Wave, 91433X, doi: [10.1117/12.2056689](https://doi.org/10.1117/12.2056689)

Planck Collaboration, Aghanim, N., Akrami, Y., et al. 2020, *A&A*, 641, A6, doi: [10.1051/0004-6361/201833910](https://doi.org/10.1051/0004-6361/201833910)

Rinaldi, P., Bonaventura, N., Rieke, G. H., et al. 2025, *ApJ*, 992, 71, doi: [10.3847/1538-4357/adfa10](https://doi.org/10.3847/1538-4357/adfa10)

Robertson, B. E., Tacchella, S., Johnson, B. D., et al. 2023, *Nature Astronomy*, 7, 611, doi: [10.1038/s41550-023-01921-1](https://doi.org/10.1038/s41550-023-01921-1)

Robertson, B. E., Johnson, B. D., Tacchella, S., et al. submitted, *ApJ*

Saxena, A., Robertson, B. E., Bunker, A. J., et al. 2023, *A&A*, 678, A68, doi: [10.1051/0004-6361/202346245](https://doi.org/10.1051/0004-6361/202346245)

Scholtz, J., Witten, C., Laporte, N., et al. 2024, *A&A*, 687, A283, doi: [10.1051/0004-6361/202347187](https://doi.org/10.1051/0004-6361/202347187)

Setton, D. J., Greene, J. E., de Graaff, A., et al. 2025, *ApJ*, 995, 118, doi: [10.3847/1538-4357/ae1500](https://doi.org/10.3847/1538-4357/ae1500)

Stefanon, M., Bouwens, R. J., Labb  , I., et al. 2021, *ApJ*, 922, 29, doi: [10.3847/1538-4357/ac1bb6](https://doi.org/10.3847/1538-4357/ac1bb6)

Sun, F., Helton, J. M., Egami, E., et al. 2024, *ApJ*, 961, 69, doi: [10.3847/1538-4357/ad07e3](https://doi.org/10.3847/1538-4357/ad07e3)

Sun, F., Fudamoto, Y., Lin, X., et al. 2025, arXiv e-prints, arXiv:2503.15587, doi: [10.48550/arXiv.2503.15587](https://doi.org/10.48550/arXiv.2503.15587)

Tacchella, S., Finkelstein, S. L., Bagley, M., et al. 2022, *ApJ*, 927, 170, doi: [10.3847/1538-4357/ac4cad](https://doi.org/10.3847/1538-4357/ac4cad)

Tacchella, S., Eisenstein, D. J., Hainline, K., et al. 2023, *ApJ*, 952, 74, doi: [10.3847/1538-4357/acdbc6](https://doi.org/10.3847/1538-4357/acdbc6)

Thomas, P. A., Lovell, C. C., Maltz, M. G. A., et al. 2023, *MNRAS*, 524, 43, doi: [10.1093/mnras/stad1819](https://doi.org/10.1093/mnras/stad1819)

Turner, C., Tacchella, S., D'Eugenio, F., et al. 2025, *MNRAS*, 537, 1826, doi: [10.1093/mnras/staf128](https://doi.org/10.1093/mnras/staf128)

Wang, K., Wang, X., & Chen, Y. 2023, *ApJ*, 951, 66, doi: [10.3847/1538-4357/acd633](https://doi.org/10.3847/1538-4357/acd633)

Wang, X., Li, Z., Cai, Z., et al. 2022, *ApJ*, 926, 70, doi: [10.3847/1538-4357/ac3974](https://doi.org/10.3847/1538-4357/ac3974)

Wechsler, R. H., & Tinker, J. L. 2018, *Annual Review of Astronomy and Astrophysics*, 56, 435, doi: [10.1146/annurev-astro-081817-051756](https://doi.org/10.1146/annurev-astro-081817-051756)

Weibel, A., de Graaff, A., Setton, D. J., et al. 2025a, *ApJ*, 983, 11, doi: [10.3847/1538-4357/adab7a](https://doi.org/10.3847/1538-4357/adab7a)

Weibel, A., Oesch, P. A., Williams, C. C., et al. 2025b, arXiv e-prints, arXiv:2507.06292, doi: [10.48550/arXiv.2507.06292](https://doi.org/10.48550/arXiv.2507.06292)

Whitler, L., Stark, D. P., Topping, M. W., et al. 2025, *ApJ*, 992, 63, doi: [10.3847/1538-4357/adfddc](https://doi.org/10.3847/1538-4357/adfddc)

Williams, C. C., Oesch, P. A., Weibel, A., et al. 2025, *ApJ*, 979, 140, doi: [10.3847/1538-4357/ad97bc](https://doi.org/10.3847/1538-4357/ad97bc)

Witstok, J., Smit, R., Saxena, A., et al. 2024, *A&A*, 682, A40, doi: [10.1051/0004-6361/202347176](https://doi.org/10.1051/0004-6361/202347176)

Witstok, J., Jakobsen, P., Maiolino, R., et al. 2025a, *Nature*, 639, 897, doi: [10.1038/s41586-025-08779-5](https://doi.org/10.1038/s41586-025-08779-5)

Witstok, J., Maiolino, R., Smit, R., et al. 2025b, *MNRAS*, 536, 27, doi: [10.1093/mnras/stae2535](https://doi.org/10.1093/mnras/stae2535)

Witten, C., Oesch, P. A., Bennett, J. S., et al. 2025a, arXiv e-prints, arXiv:2511.05647, doi: [10.48550/arXiv.2511.05647](https://doi.org/10.48550/arXiv.2511.05647)

Witten, C., Oesch, P. A., McClymont, W., et al. 2025b, arXiv e-prints, arXiv:2507.06284, doi: [10.48550/arXiv.2507.06284](https://doi.org/10.48550/arXiv.2507.06284)

Wu, Z., Eisenstein, D. J., Johnson, B. D., et al. 2025, *ApJ*, 992, 212, doi: [10.3847/1538-4357/ae01a1](https://doi.org/10.3847/1538-4357/ae01a1)

Zahn, O., Lidz, A., McQuinn, M., et al. 2007, *The Astrophysical Journal*, 654, 12, doi: [10.1086/509597](https://doi.org/10.1086/509597)